Melt-rock interactions, deformation, hydration and seismic properties in the sub-arc lithospheric mantle inferred from xenoliths from seamounts near Lihir, Papua New Guinea

Vincent Soustelle, Andrea Tommasi, Sylvie Demouchy, Leander Franz

Melt-rock interactions, deformation, hydration and seismic properties in the sub-arc lithospheric mantle inferred from xenoliths from seamounts near Lihir, Papua New Guinea

Vincent Soustelle [a,b,*], Andréa Tommasi [b], Sylvie Demouchy [b], Leander Franz [c]

[a] Bayerisches Geoinstitut, Universität Bayreuth, Universitätstrasse 30, D-95440 Bayreuth, Germany
[b] Géosciences Montpellier, Université Montpellier II & CNRS, CC60, Place E. Bataillon, 34095 Montpellier cedex 5, France
[c] Mineralogisch-Petrographisches Institut, Universität Basel, Bernoullistrasse 30, 4056 Basel, Switzerland

This study analyses the interactions between deformation and reactive fluid and melt percolation, and their ef-fects on sub-arc mantle seismic properties based on microstructural observations on mantle xenoliths extracted by the Tubaf and Edison seamounts close to the Lihir Island, in the Papua New Guinea archipelago. These xeno-liths sample an oceanic lithosphere, which has experienced high-temperature deformation in the presence of fluids or melts. This was followed by metasomatism under static conditions. Syn-kinematic percolation of reac-tive Si-rich melts or fluids in peridotites has produced pyroxene-enrichment, grain size reduction, and dispersion of olivine crystal preferred orientation (CPO). Fourier transform infrared spectroscopy analyses show that olivine has very low water contents (1–4 wt. ppm H_2O), similar to spinel peridotites from other subduction zones. These low values may record both low water solubility in olivine at low pressure and dehydration during transport and exhumation. Water contents in pyroxenes are highly variable and likely result from spatially heterogeneous melt or fluid percolation. Analysis of olivine CPO indicates dominant activation of both (010)[100] and (001)[100] slip systems, which are characteristic of deformation under high temperature, low stress, low pressure and low to moderate hydrous conditions. Fast S-wave polarization and P- and Rayleigh propagation directions are thus par-allel to the mantle flow direction. The pyroxene enrichment by melt-rock reactions is accompanied by dispersion of olivine CPO and induces a significant decrease of the maximum S-wave and P-wave anisotropy in the perido-tites. The calculated seismic properties also show that the lowest Vp/Vs ratios (<1.7) mapped in fore-arc mantle may only be explained by taking in consideration the CPO-induced elastic anisotropy of the peridotites.

1. Introduction

The supra-subduction mantle is the site of a series of petrological processes, ranging from dehydration of subducted slab to partial melting and metasomatism in the wedge. These processes may affect the peridotites' composition, their rheology, and, by consequence, the flow patterns and seismic properties in the mantle wedge. Both the presence of small melt fractions and the incorporation of water in olivine can strongly reduce the strength of mantle rocks (Blacic, 1972; Boudier, 1991; Demouchy et al., 2012; Hirth and Kohlstedt, 1995a, 1995b; Karato et al., 1986; Mackwell et al., 1985; Mei and Kohlstedt, 2000a, 2000b; Mei et al., 2002; Zimmerman and Kohlstedt, 2004). They may also modify the mechanisms of plastic deformation in olivine and the relation between seismic anisotropy and mantle flow (Holtzman et al., 2003b; Jung and Karato, 2001). Recent studies in peridotite massifs and xenoliths also highlighted that reactive melt percolation in the upper mantle may lead to enrichment in pyroxene and dispersion of the olivine crystal preferred orientation (CPO), producing a significant reduction of the peridotites seismic anisotropy (Le Roux et al., 2008; Soustelle and Tommasi, 2010; Soustelle et al., 2009, 2010).

The effects of melt and fluid percolation and hydration on mantle wedge composition and physical properties may be observed using seismological observations such as Vp/Vs ratio, attenuation and seismic anisotropy (*e.g.*, Karato, 2002; Karato and Jung, 1998; Nakajima and Hasegawa, 2004; Sato et al., 1989; Wagner et al., 2006; Zhang et al., 2004). However, processes other than the presence of melt, fluid or hydration may produce similar seismic signatures. Regarding seismic anisotropy, observation of trench parallel fast shear-waves polarization direction may result from deformation of hydrated olivine (Jung and Karato, 2001), from deformation in the presence of melt (Holtzman et al., 2003a), from trench-parallel mantle flow (*e.g.*, Kneller and van Keken, 2008), or from serpentinization in the subducting slab or in the mantle wedge (*e.g.*, Boudier et al., 2010; Faccenda et al., 2008). Variation of Vp/Vs ratios may be explained by the presence of melt, fluid or variations in composition, but they may also be produced by the intrinsic

* Corresponding author at: Bayerisches Geoinstitut, Universität Bayreuth, Universitätstrasse 30, D-95440 Bayreuth, Germany. Tel.: +49 921 55 3878; fax: +49 921 55 3769.
E-mail address: Vincent.Soustelle@uni-bayreuth.de (V. Soustelle).

anisotropy of the mantle wedge (Soustelle and Tommasi, 2010). Finally, seismic attenuation is sensitive to melt, to hydration in the mantle minerals, as well as to temperature variations (*e.g.*, Hammond and Humphreys, 2000; Karato and Jung, 1998; Schmeling, 1985). Combining geophysical soundings with direct studies on mantle rocks such as peridotite xenoliths is therefore essential to build the most accurate models of the mantle wedge geodynamics.

Direct samples from the mantle wedge may be extracted by subduction-related calc-alkaline volcanism, but they are extremely rare. Moreover, most previous studies on subduction zone mantle xenoliths have focused on geochemical and petrological processes (*e.g.*, Arai and Kida, 2000; Bénard and Ionov, 2009; Gregoire et al., 2001; Ionov, 2010; Ionov and Seitz, 2008; Ishimaru et al., 2007; McInnes et al., 2001). Fewer studies, all based on xenoliths from the Avacha volcano in the Kamchatka, have analysed their deformation and seismic properties (Michibayashi et al., 2009; Soustelle and Tommasi, 2010; Soustelle et al., 2010). Here we present a detailed microstructural study, as well as measurement of CPO and of water contents in olivine, orthopyroxene and clinopyroxene for 8 ultramafic xenoliths (7 peridotites and 1 olivine clinopyroxenite) from two seamounts off the coast of the Lihir Island (Fig. 1). They sample the lithospheric mantle above a stalled Tertiary subduction zone in the Bismarck Archipelago, NE of Papua New Guinea. We analyse the relations between deformation, fluids and melt percolation, and hydration in the sub-arc mantle wedge and compute the seismic properties of these mantle xenoliths to evaluate the impact of these processes on seismic data in subduction settings.

2. Geological setting

The studied samples are mantle xenoliths of 4 to 10 cm in diameter, which were hosted in trachybasalts collected at the top of two submarine volcanoes, the Tubaf (3°15.25′S, 152°32.50′E, 1280 m below sea level) and the Edison (3°19.05′S, 152°34.90′E, 1450 m below sea level) seamounts (Franz et al., 2002; Herzig et al., 1994, 1998). These seamounts crop out southward of Lihir Island in the Bismarck Archipelago, NE of Papua New Guinea (Fig. 1).

This region records a complex geodynamic evolution. Southwestward subduction of the Pacific plate beneath the Bismarck microplate along the Manus–Kilinailau trench produced voluminous calc-alkaline arc volcanism during the Oligocene and Miocene. Around 15 My, collision of the Ontong-Java plateau with the trench resulted in subduction reversal. This led to the formation of the currently active New Britain trench (NNW- to NNE-dipping), which accommodates the subduction of the Solomon Sea microplate under the Bismarck microplate (Coleman and Kroenke, 1981). Back-arc spreading, contemporaneous to the subduction, occurs in the Manus basin leading to the separation of a North and a South Bismarck microplates (Fig. 1).

Both Tubaf and Edison seamounts belong to the Tabar–Lihir–Tanga–Feni (TLTF) volcanic island chain located NE of the New Ireland Island in the North Bismarck microplate (Fig. 1). The volcanic activity in this chain started 3.6 my ago (McInnes, 1992; Rytuba et al., 1993) and the most recent on land eruption occurred in the Feni Island around 2.3 ky ago (Licence et al., 1987). This high-K calc-alkaline volcanism has been interpreted as linked to lithospheric thinning of the Bismarck microplate in response to the opening of the Manus back-arc basin (*e.g.*, Taylor, 1979). Based on geochemical data, McInnes and Cameron (1994) proposed that the strong metasomatism of the Bismarck microplate during the subduction of the Pacific plate in the Tertiary had also a strong influence on the melt generation.

3. Previous petrological and geochemical studies

Two dunites, three harzburgites, two lherzolites and one olivine clinopyroxenite (Table 1) were selected among a larger xenolith

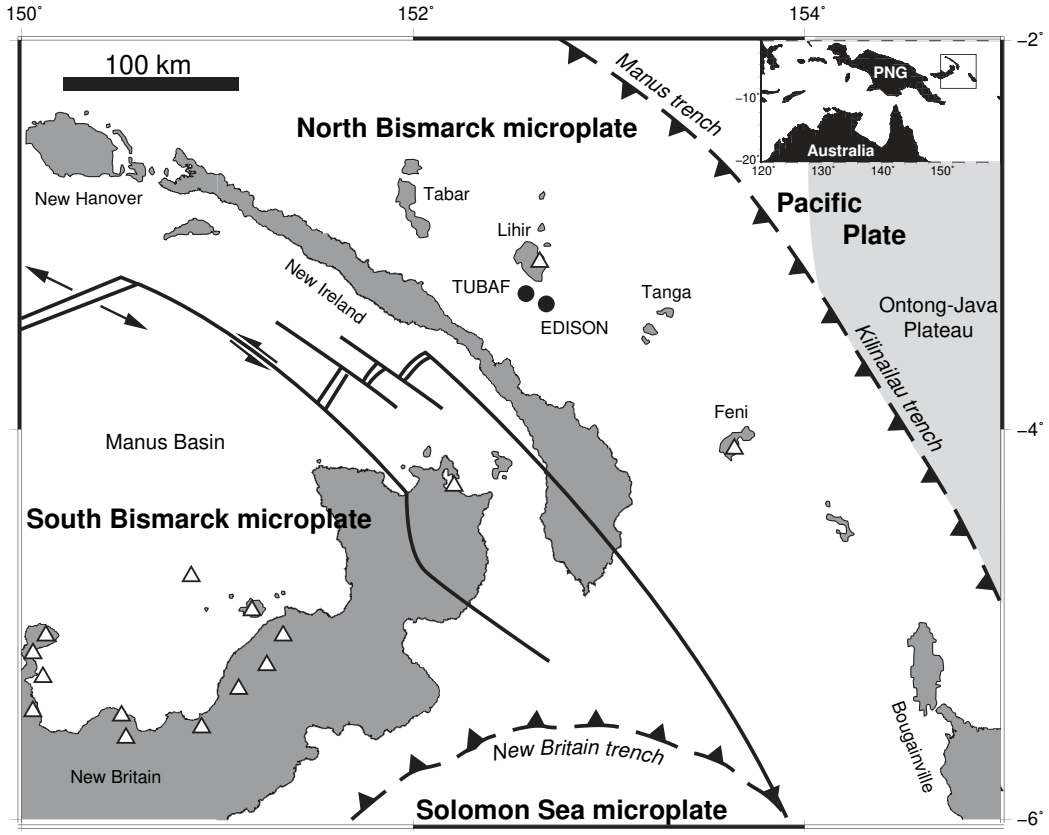

Fig. 1. Map of the Bismarck Archipelago with the Tubaf and Edison seamount location; insert shows the position of this Archipelago compared to Papua-New-Guinea (modified from Franz et al., 2002).

Table 1
Modal composition and microstructural data.

Sample	Type	Mode (wt.%)			Ol mean grain size (μm)	CPO pattern	J ol	J opx	J cpx	Ol aspect ratio
		Ol	Opx	Cpx						
55-2B[a]	Dunite	97	0	3	696	Axial-[100]	10.46	–	–	1.77
54-2A	Dunite	93	0	5	865	Axial-[100]	9.25	–	–	1.9
56-2A	Harzburgite	85	13	1	653	Orthorhombic	7.79	–	–	1.83
55-2A[a]	Harzburgite	78	20	2	593	Axial-[100]	5.24	3.55	–	1.79
54-2D	Lherzolite	67	16	15	441	Axial-[100]	4.13	2.06	–	1.77
56-2H[a]	Lherzolite	70	24	6	586	Axial-[100]	3.44	2.34	5.06	1.92
56-2T	Harzburgite	72	26	2	518	Orthorhombic	3.34	1.85	–	1.98
33-2A	Ol-clinopyroxenite	16	1	83	376	Orthorhombic	3.25	–	3.05	1.5

[a] Modal composition from EBSD map.

collection that has been the subject of a detailed petrological and geochemical study, which includes petrographic descriptions, major and trace element whole-rock analyses, and mineral electron microprobe analyses (Franz et al., 2002). Petro-geochemical data on harzburgite xenoliths from the same localities were also reported by Gregoire et al. (2001) and McInnes et al. (2001).

Based on observation of retrograde zoning and of exsolution lamellae of spinel in olivine, Franz and Wirth (2000) proposed that these xenoliths record a cooling history that possibly started at a mid-ocean ridge or back-arc basin spreading-centre. Ortho- and clinopyroxene also show chemical zoning and exsolution lamellae typical of lithospheric cooling, which probably occurred as the mantle lithosphere cooled and thickened with increasing age-distance from the ridge (Franz et al., 2002).

The small modal amount of primary clinopyroxene in these peridotites indicates a strong depletion of the lithospheric mantle of the Bismarck microplate (Franz et al., 2002). This strong depletion is also observed in another suite of xenoliths from the same localities, which display similar features to our samples. These xenoliths are all harzburgites strongly depleted in Al_2O_3, CaO, and Na_2O and enriched in Ni and Co and were interpreted as solid residues resulting from high degree of partial melting (Gregoire et al., 2001; McInnes et al., 2001).

The Tubaf and Edison peridotite xenoliths were submitted to extensive medium to high temperature metasomatism after cooling and incorporation into the mantle lithosphere (Franz et al., 2002; Gregoire et al., 2001). Most peridotites are veined and/or display evidence for growth of metasomatic orthopyroxene and clinopyroxene, spinel, phlogopite, or amphibole. Metasomatic orthopyroxene and clinopyroxene form aggregates of minute needle-like and rounded crystals, respectively, which may be easily distinguished from primary, coarser grained orthopyroxene and clinopyroxene. Petrological data point to a hydrous fluid phase with variable amount of dissolved alkali cations as the metasomatic agent (Franz et al., 2002; Gregoire et al., 2001). Xenoliths without any visible metasomatic features also record a distinct metasomatic alteration as indicated by their elevated light rare earth element (LREE) patterns (Franz et al., 2002). This metasomatism probably occurred in a supra-subduction zone setting during the subduction of the Pacific Plate underneath the Bismarck microplate. This interpretation is corroborated by oxygen barometry on the metasomatic veins, which revealed a high oxygen fugacity ($D\log(fO_2)^{FMQ}$ values of 0.4–4.3), typical for hydrous fluids derived from the dehydrated subducted slab (Franz et al., 2002; McInnes et al., 2001). Based on mineral major- and trace-element compositions, Franz and Romer (2010) proposed that metasomatic veins in the ultramafic xenoliths from the Tubaf seamount are associated to two distinct subduction-related events, with metasomatic agents mobilized from both subducted Solomon Sea Microplate and Pacific Plate.

Geothermometry on primary pyroxenes from spinel peridotites (rim composition) using the calibration of Brey and Köhler (1990) yields equilibrium temperatures of 730–980 °C. Intersecting the K_D-lines of this geothermometer with the present day geothermal gradient of the region (corresponding to a surface heat flow of 60 mW/m^2; Pollack and Chapman, 1977) yields pressures between 1.3 and 1.8 GPa (~43–60 km), which corresponds to the spinel-peridotite stability field (Franz et al., 2002). Temperatures of 770–1190 °C are obtained for the metasomatic veins using the olivine–spinel geothermometer of Ballhaus et al. (1991). The sampling of plagioclase–lherzolites and olivine clinopyroxenites in these localities also evidences metasomatism at shallow lithospheric levels. PT conditions for this latter metasomatic overprint were estimated at 680–780 °C and 0.2–0.3 GPa using different thermobarometers (Franz et al., 2002).

Among the studied xenoliths, there is one olivine clinopyroxenite (33-2A), which is crosscut by hornblende-phlogopite veins (5 mm wide). Based on its peculiar mineralogy and texture and on its geochemistry, this sample (33-2A) has been interpreted as a magmatic cumulate. A PT-estimate using a combination of the olivine–spinel geothermometer of Ballhaus et al. (1991) and the Ca-in-olivine geobarometer of Köhler and Brey (1990) points to a shallow lithospheric origin at elevated temperatures (950 ± 30 °C at 1.3 ± 0.4 GPa).

Franz et al. (2002) have discussed in depth the influence of the host trachybasalt on the studied xenoliths. They have shown that the metasomatic veins do not widen towards the rim of the rocks. They bear an equilibrium mineral assemblage, which in part incorporates high-pressure phases like garnet. Some samples display dynamic recrystallization and mineral alignment in these veins pointing to deformation processes (Franz et al., 2002), which would not be possible during the uplift in the magma or across the volcanic edifice. Furthermore, the mineral zoning in these veins point to relatively long lasting processes (Franz et al., 2002). These facts as well as the thermobarometry data clearly demonstrate that the formation of most veins occurred prior to the interaction with the trachybasaltic host magma. However, some xenoliths show a type of irregular metasomatism, which resulted in the formation of high-temperature pyroxenes and late amphiboles. Franz et al. (2002) interpreted the high-temperature pyroxenes as due to the interaction between the host magma and the xenolith and the secondary amphiboles due to a late hydrothermal overprint. The same processes may account for crystallization of the tertiary pyroxenes, which overgrow the primary or secondary pyroxenes (see Section 4 for the definition of the pyroxene types) and show no indication for mineral alignment.

4. Microstructural observations

The studied peridotite xenoliths display variable textures. According to the nomenclature of Passchier and Trouw (2005) based on Moore (1970), we observed a seriate (a complete gradation of fine- to coarse-grained crystals) polygonal to interlobate (with irregular, lobate grain boundaries) texture in the two dunites (Fig. 2a) and one harzburgite (56-2A). The remaining harzburgites and one lherzolite (56-2H) display a seriate interlobate texture (Fig. 2c and e), whereas the lherzolite 54-2D is equigranular polygonal.

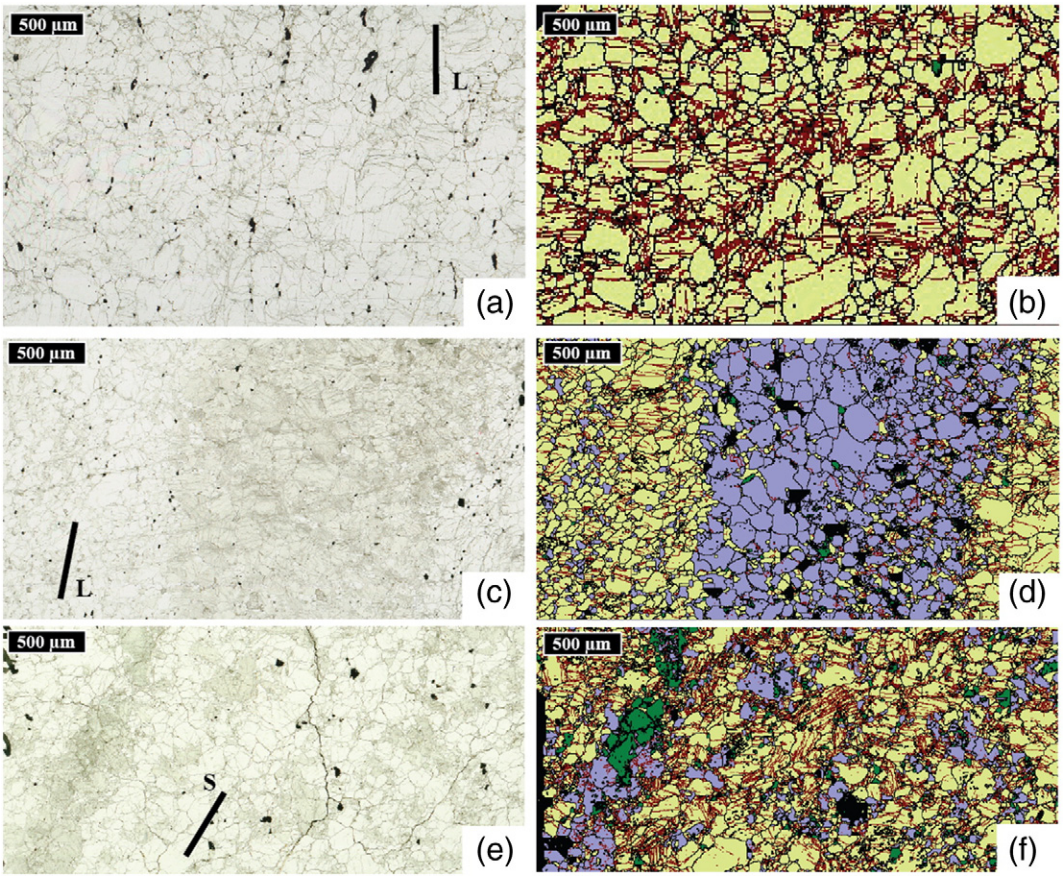

Fig. 2. Photomicrographs in plane polarized light (a, c, e) and EBSD maps (b, d, f) illustrating typical structures and microstructures, as well as the parallelism between deformation structures (S and L) and pyroxene distribution in the Lihir peridotite xenoliths. The lineation (L) is underlined by spinel (black) alignments in samples 54-2A (a) and 56-2T (b). The foliation (S) in sample 56-2H is constrained by the analysis of the olivine CPO (c). In the EBSD maps, yellow: olivine, blue: orthopyroxene, green: clinopyroxene, black: not indexed, black lines: phase and grain boundaries, maroon lines: subgrain boundaries.

In the seven peridotites, the trace of the foliation and the lineation are marked by spinel trails (Fig. 2a and c) and a weak elongation of olivine crystals, which have apparent aspect ratios around 1:2 (Table 1). The harzburgites and lherzolites 56-2T, 56-2H and 55-2A show a discontinuous modal layering marked by enrichment in orthopyroxene and minor clinopyroxene in 0.5–1.5 mm wide bands parallel to the spinel trails (Fig. 2b and c).

The olivine average grain size in the peridotites ranges from 450 to 850 µm (Table 1) and is roughly positively correlated with the olivine modal proportion in the sample (Fig. 3). Within and in the vicinity of the pyroxene-rich bands or lenses, the olivine grain size is finer ($\leq$300 µm, Fig. 4a) than in orthopyroxene-poor levels. Olivine crystals display anhedral to subhedral shapes. The olivine–olivine grain boundaries range from interlobate to smoothly curved (Fig. 4a) and may be locally straight, leading to more polygonal crystal shapes, forming 120° triple junctions (Fig. 4b). In contrast, the olivine–pyroxene grain boundaries are generally lobate (Figs. 4a and 5a–d). This difference is likely responsible for the texture variation from polygonal to interlobate with the increasing of pyroxene proportion, *i.e.* from dunite to lherzolite. Olivine crystals display a strong undulose extinction and closely-spaced subgrain boundaries (Fig. 4b and c).

Pyroxene microstructures can be divided in 3 groups:

(1) The primary pyroxenes described by Franz et al. (2002) (referred to as primary orthopyroxenes or clinopyroxenes subsequently) are coarse crystals (>500 µm) that occur isolated or in aggregates (Fig. 5a and b). Isolated crystals have anhedral shapes with interlobate grain boundaries and/or enclose surrounding olivine crystals (Fig. 5b and c). Within an aggregate, pyroxenes may display curved to straight grain boundaries and form 120° triple junctions. They often have a turbid aspect due to a large amount of fluid and solid inclusions (Fig. 5a and c). Primary orthopyroxenes bear clinopyroxene exsolutions and *vice-versa*. Both pyroxenes also contain minor spinel exsolutions. They often show undulose extinction in their cores (Fig. 5a) and orthopyroxene may be kinked (Fig. 5b).

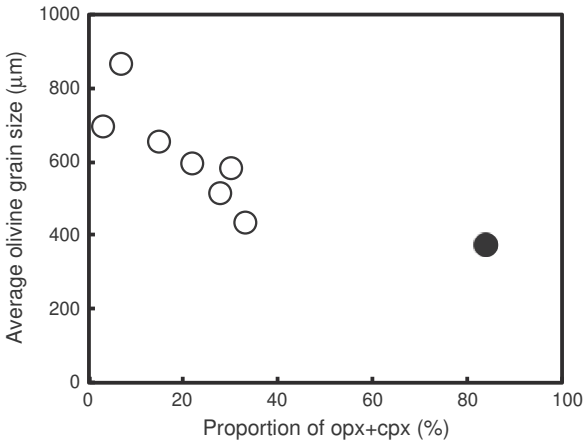

Fig. 3. Average olivine grain size calculated from EBSD map in relation to the pyroxene content.

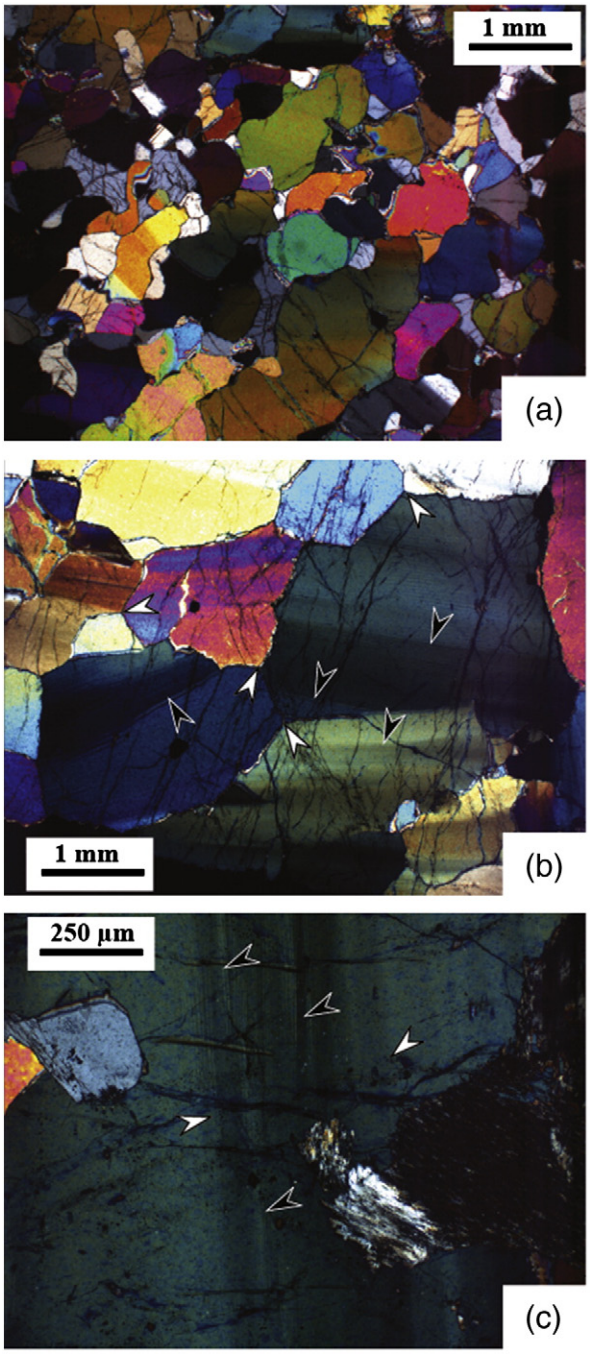

Fig. 4. Photomicrographs in cross-polarized light: (a) Zone of fine-grained olivine crystals and fine interstitial secondary orthopyroxene (see text) close to the contact with the orthopyroxenite vein that crosscuts peridotite sample 56-2T. (b) Subgrain boundaries (black arrows) and 120° triple junction (white arrows) in olivine in sample 54-2A. (c) Subgrain boundaries in olivine in sample 56-2A, indicated by white and black arrows.

(2) The pyroxene-rich bands and lenses are composed by small (<500 µm) orthopyroxenes and rarer clinopyroxene crystals (referred to as secondary orthopyroxene or clinopyroxene subsequently), which display anhedral shapes with very sinuous grain boundaries. They may have film-like or interstitial shapes along olivine–olivine interfaces and at triple junctions (Fig. 5b and d). These secondary pyroxenes are usually optically clear crystals, free of intracrystalline deformation features and exsolutions.

(3) Finally, a third type of pyroxenes, subsequently referred as tertiary orthopyroxene or clinopyroxene, corresponds to the secondary metasomatic orthopyroxenes and recrystallized clinopyroxenes previously described by Franz et al. (2002). They form cloudy aggregates composed of fine-grained rounded (<200 µm) to acicular (<50 µm wide and <200 µm long) pyroxene crystals (Fig. 5e and g). These tertiary pyroxenes occur in metasomatic orthopyroxenite (Fig. 5e) and clinopyroxene-ol-phlogopite (Fig. 5f and g) veins (Franz et al., 2002). These veins crosscut all minerals and their deformation-related microstructures and form an interconnected, anastomozing network. When crosscutting a primary or secondary orthopyroxene or clinopyroxene, the veins tend to widen, forming diffuse reaction zones characterized by recrystallization of the primary and secondary pyroxenes. In pyroxene-rich areas of the studied lherzolites and harzburgites, the mineralogical assemblages forming the metasomatic veins also tend to occur as thin films along grain boundaries.

The olivine clinopyroxenite 33-2A is composed of coarse (>500 µm) anhedral to subhedral clinopyroxene and small (<400 µm) anhedral olivine crystals, displaying an interlobate texture (Table 1). Clinopyroxene and olivine show no evidence of intracrystalline deformation. Numerous lamellae of hornblende and spinel are found in the clinopyroxenes. Two 5 mm wide hornblende–phlogopite veins mainly formed of coarse (500–1000 µm) subhedral hornblende crystals crosscut this sample; the vein walls are straight and the composing crystals free of deformation microstructures.

5. Crystal preferred orientations

5.1. Analytical procedure

Mineral crystal preferred orientations (CPO) were determined by indexation of electron-backscattered diffraction (EBSD) patterns by using a scanning electron microscope (SEM) coupled with EBSD system at the SEM-EBSD facility at Geosciences Montpellier (France). EBSD patterns are generated by interaction of a vertical incident electron beam with a carefully polished thin section tilted at 70° in a scanning electron microscope JEOL JSM 5600. The diffraction pattern is projected onto a phosphor screen and recorded by a digital CCD camera. The image is then processed and indexed in terms of crystal orientation using the CHANNEL5 software from Oxford Instruments HKL.

For each sample, we obtained crystallographic orientation maps covering almost entirely the thin section (usually 35 mm long and 20 mm wide) with sampling steps of 100, 75, or 50 µm, depending on the grain size (sampling steps are always at least 1/4 of the average grain size). Indexation rates in the raw maps range from 50 to 80%. In general, indexation rates are lower for the pyroxenes than for olivine. Tertiary pyroxenes, due to the fine-grained size of the individual crystals composing the aggregates, are poorly indexed (<50%). Very low indexation rates were also obtained in the metasomatic veins.

Post-acquisition data treatment allowed to further increase the indexation rate by:

(i) Filling the non-indexed pixels, which have up to 8 identical neighbours with this orientation.
(ii) Repeating this operation using respectively 7, 6, and 5 identical neighbours.
(iii) Identifying the grains area, *i.e.*, continuous domains characterized by an internal misorientation <10°, and
(iv) within each olivine crystal, searching and correcting for systematic indexation errors due to the olivine hexagonal pseudo-symmetry, which results in similar diffraction patterns for orientations differing by a rotation of 60° around [100].

At each step, the resulting orientation maps were verified by comparison with optical images to avoid over-extrapolation of the data.

Because of the xenoliths small size and irregular geometry, the thin-sections were not systematically cut parallel to the lineation and normal

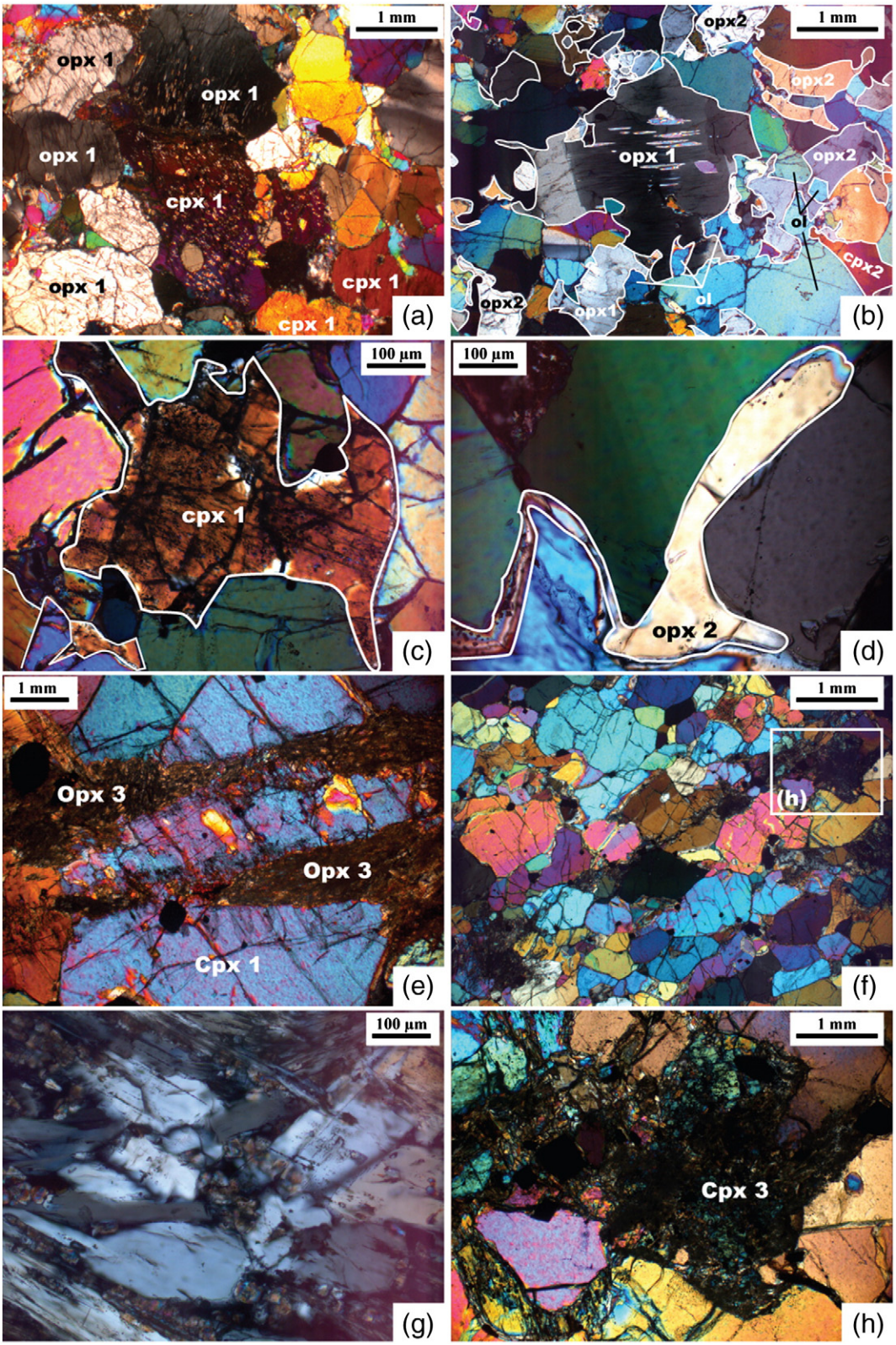

Fig. 5. Photomicrographs in cross-polarized light illustrating the orthopyroxene and clinopyroxene textures. (a) Exsolution-bearing coarse primary orthopyroxene and clinopyroxene displaying a turbid aspect and undulose extinction in a pyroxene-rich vein in the sample 56-2H. (b) Coarse primary orthopyroxene displaying kink-bands and highly indented grain boundaries next to smaller, undeformed secondary orthopyroxene and clinopyroxene grains in sample 55-2A. (c) Fine corroded primary clinopyroxene in sample 54-2D. (d) Secondary orthopyroxene crystallized on olivine grain boundaries in sample 55-2A. (e) Primary clinopyroxene crosscut by metasomatic veins containing tertiary orthopyroxene in sample 54-2D. (f) Metasomatic veins crosscutting olivine crystals and their microstructures, and forming aggregate of clinopyroxene-ol-phlogopite at the contact with a primary clinopyroxene; sample 54-2D. (g) Details of a fine-grained acicular and prismatic orthopyroxene aggregate forming the tertiary orthopyroxene in sample 56-2A. (h) Detail of panel f showing tertiary clinopyroxene aggregates.

to the foliation, but all CPO were reoriented to have the maximum concentrations of olivine [100] and [010] axes parallel to the E–W and N–S directions, respectively. This allows a straightforward comparison between the different samples of CPO as well as to previously published data. In order to avoid over-representation of large crystals, CPO is plotted as one measurement per grain (average orientation of the crystal).

The J-index, which is the volume-averaged integral of the squared orientation densities (Bunge, 1982), is used to quantify the CPO strength. It has a value of unity for a random CPO and tends to infinity for single crystal, but most of olivine CPO in natural samples show J-index values between 2 and 20 with a peak around 8 (Ben Ismail and Mainprice, 1998; Tommasi et al., 2000). In the studied peridotites, the J-index ranges between 3.3 and 10.2.

5.2. Results

The studied mantle xenoliths display clear olivine CPO (Fig. 6). Most samples show well-developed axial-[100] patterns characterized by a strong point concentration of the [100] axes. [010] and [001] axes are distributed in a girdle distribution normal to the [100] maximum, with two maxima roughly normal to each other. The [010] maximum is usually stronger than the [001] one. Three samples (56-2A, 56-2T, and 33-2A) display, however, a more orthorhombic olivine CPO characterized by point concentrations of the three main crystallographic axes. The concentration of the [100] axes is usually the strongest (except in the olivine clinopyroxenite 33-2A), and the [001] axes are the most dispersed. When observed, the mineral lineation is sub-parallel to the maximum concentration of the [100] axes and the foliation normal to the maximum concentration of [010].

There is no correlation between olivine CPO symmetry and its strength, as characterized by the J-index (Fig. 6). The olivine CPO strength decreases, however, with an increasing proportion of pyroxenes (Fig. 7). It is the lowest in the olivine clinopyroxenite (3.3) and the highest in the dunites (>9). A high J-index (7.8) is also observed in sample 56-2A, which has a dunite-like composition (due to its habitus, we interpret that orthopyroxene in this sample results from metasomatism).

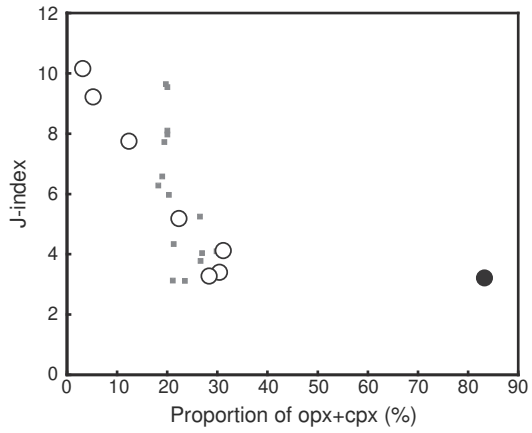

Fig. 7. J index for olivine calculated using one orientation datum per grain versus the modal proportion of pyroxene in each sample. White and black circles are peridotites and clinopyroxenites from this study, respectively, and the small grey squares are data of peridotite xenoliths from Avacha volcano, Kamchatka (Soustelle et al., 2010).

Orthopyroxene and clinopyroxene display more dispersed CPO. Even when >100 grains were measured, it is difficult to distinguish a clear CPO pattern, since the pole figures often display multiple weak maxima (Fig. 6). This problem is due to the poor indexation of the pyroxenes, due to altered surfaces and, for the tertiary pyroxenes, their fine-grained character, which both lead to single crystals being recorded as multiple patches with a similar orientation. This indexation bias leads to an over-representation of this orientation in the pole figure. In harzburgite 55-2A and, in a lesser extent, lherzolite 54-2D, orthopyroxene has a weak, but clear CPO, characterized by a concentration of [001] axes at low angle to the olivine [100] maximum and to the lineation. In harzburgite 55-2A, [100] axes are aligned normal to the foliation, that is close to the olivine [010] maximum, whereas in lherzolite

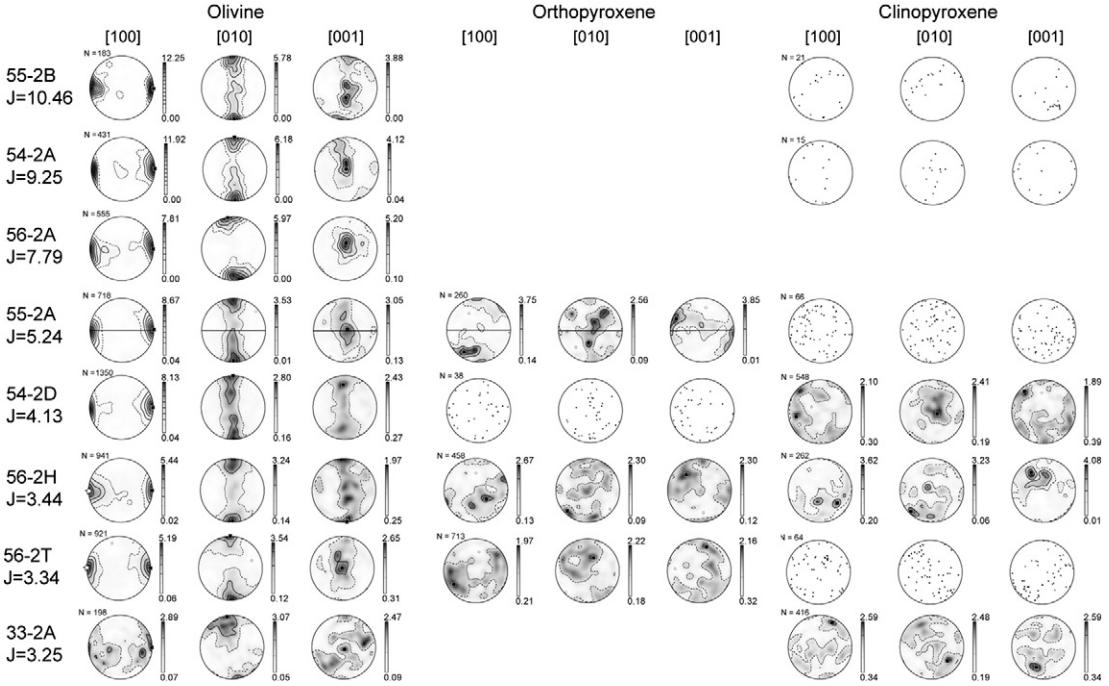

Fig. 6. Olivine, orthopyroxene and clinopyroxene crystal preferred orientations. Lower hemisphere, equal area stereographic projections, contours at one multiple of uniform distribution. All the data were rotated to have the olivine [100] maximum in the E–W horizontal direction and the [010] maximum close to the N–S horizontal direction. Lineation and foliation, when observed, are indicated by a star and a continuous line, respectively.

54-2D [010] axes tends to form a wide girdle at high angle to the lineation. Clinopyroxene CPO in both samples is more dispersed. The remaining peridotites (56-2H & 56-2-T) have very weak orthopyroxene CPO, which are not consistent with the olivine CPO. The clinopyroxene CPO in these samples either mimics the orthopyroxene CPO (56-2H) or displays an unusual correlation to it ([001] cpx is subparallel to [100] opx). Finally, olivine clinopyroxenite 33-2A has a very weak clinopyroxene CPO oblique to the olivine one.

6. Water contents in olivine and pyroxenes

6.1. Analytical procedure

Unpolarized Fourier transform infrared (FTIR) absorption spectra of olivine and orthopyroxene were obtained on doubly polished sections with a thickness of 280 to 353 μm (Table 2). The sections have been left in an acetone bath for at least 12 h in order to remove any residual glue. We selected optically crack- and inclusion-free grains. Measurements were performed using a Bruker IFS66v spectrometer coupled with a Bruker microscope type A590 or a Bruker Hyperion microscope at University of Montpellier 2. Both microscopes were equipped with all-reflecting Cassegranian optics, a condenser, and an ×15 objective. Analyses were made at room pressure and temperature, and under dry and clean air flux. Unpolarized middle infrared measurements were generated using a Globar light source, a KBr beam splitter, and analysed with a high sensitivity MCT (mercury–cadmium–telluride) detector cooled by liquid nitrogen. Spectra were acquired with a resolution of 4 cm^{-1} and 300 scans were accumulated for each spectrum, except for 56-2H minerals (100 scans). Circular or squared apertures were used with a diameter or a length side of 105 μm or ~100 μm, respectively (Table 2). Measurements in orthopyroxene and clinopyroxene were hindered by the large amount of inclusions in the coarse crystals and by the fine-grained texture of the orthopyroxene aggregates, but several clean spectra could be obtained in most samples.

Table 2
Water contents in olivines, orthopyroxenes and clinopyroxenes measured by FTIR.

Sample	Mineral	Microscope	Aperture size (mm)[a]	Section thickness (cm)	Water content (wt. ppm H_2O)[b]	Water content ($H/10^6$ Si)[b]	Water content (wt. ppm H_2O)[c]	Water content (wt. ppm H_2O)[d]
33-2A	Cpx-1	Hyperion	0.1 × 0.1	0.0320	204.0	2393.7	–	–
33-2A	Cpx-2	Hyperion	0.1 × 0.1	0.0321	178.0	2090.7	–	–
33-2A	Cpx-3	Hyperion	0.1 × 0.1	0.0322	117.0	1370.3	–	–
33-2A	Cpx-4	Hyperion	0.1 × 0.1	0.0323	157.0	1845.4	–	–
33-2A	Mean-cpx	–	–	–	166.0	1954.0	–	–
54-2A	Ol-1	Hyperion	0.1 × 0.1	0.0315	1.0	22.52	2.9	1.8
54-2D	Ol-1	Hyperion	0.1 × 0.1	0.0355	2.0	35.3	5.8	3.6
54-2D	Ol-2	Hyperion	0.1 × 0.1	0.0355	1.0	21.2	2.9	1.8
54-2D	Ol-3	Hyperion	0.1 × 0.1	0.0355	1.0	18.3	2.9	1.8
54-2D	Cpx-1	Hyperion	0.1 × 0.1	0.0355	77.0	902.2	–	–
54-2D	Cpx-2	Hyperion	0.1 × 0.1	0.0355	78.0	922.4	–	–
54-2D	Mean-ol	–	–	–	1.3	24.6	3.9	2.4
54-2D	Mean-cpx	–	–	–	77.5	912.3	–	–
55-2A	Ol-1	Type A590	0.105	0.0280	4.0	68.2	11.6	7.2
55-2A	Ol-2	Type A590	0.105	0.0280	3.0	51.1	8.7	5.4
55-2A	Ol-3	Type A590	0.105	0.0280	2.0	31.6	5.8	3.6
55-2A	Ol-4	Type A590	0.105	0.0280	2.0	31.7	5.8	3.6
55-2A	Ol-5	Type A590	0.105	0.0280	3.0	45.4	8.7	5.4
55-2A	Ol-6	Type A590	0.105	0.0280	2.0	25.5	5.8	3.6
55-2A	Ol-7	Type A590	0.105	0.0280	1.0	24.2	2.9	1.8
55-2A	Ol-8	Type A590	0.105	0.0280	1.0	23.2	2.9	1.8
55-2A	Cpx-1	Type A590	0.120	0.0280	169.0	2027.8	–	–
55-2A	Cpx-2	Type A590	0.120	0.0280	253.0	3044.7	–	–
55-2A	Mean-ol	–	–	–	2.2	34.1	6.5	4.0
55-2A	Mean-cpx	–	–	–	216.0	2462.0	–	–
56-2A	Ol-1	Hyperion	0.1 × 0.1	0.0348	2.0	30.0	5.8	3.6
56-2A	Ol-3	Hyperion	0.1 × 0.1	0.0348	1.0	18.1	2.9	1.8
56-2A	Ol-4	Hyperion	0.1 × 0.1	0.0348	1.0	19.5	2.9	1.8
56-2A	Opx-1	Hyperion	0.1 × 0.1	0.0348	431.0	4890.1	–	–
56-2A	Mean-ol	Hyperion	–	–	1.3	23.8	3.9	2.4
56-2H	Ol-1	Type A590	0.105	0.0330	2.0	32.9	5.8	3.6
56-2H	Ol-2	Type A590	0.105	0.0330	2.0	36.5	5.8	3.6
56-2H	Ol-3	Type A590	0.105	0.0330	2.0	35.4	5.8	3.6
56-2H	Ol-4	Type A590	0.105	0.0330	2.0	26.3	5.8	3.6
56-2H	Ol-5	Type A590	0.105	0.0330	2.0	26.985	5.8	3.6
56-2H	Cpx-1	Type A590	0.105	0.0330	378.0	4442.5	–	–
56-2H	Cpx-2	Type A590	0.105	0.0330	382.0	5875.2	–	–
56-2H	Opx-1	Type A590	0.105	0.0330	249.0	2771.0	–	–
56-2H	Mean-ol	–	–	–	2.0	30.944	5.8	3.6
56-2H	Mean-cpx	–	–	–	380.0	4469.9	–	–
56-2T	Ol-1	Hyperion	0.1 × 0.1	0.0353	1.0	17.9	2.9	1.8
56-2T	Ol-2	Hyperion	0.1 × 0.1	0.0353	1.0	19.8	2.9	1.8
56-2T	Ol-3	Hyperion	0.1 × 0.1	0.0353	2.0	32.4	5.8	3.6
56-2T	Opx-1	Hyperion	0.1 × 0.1	0.0353	39.0	447.1	–	–
56-2T	Opx-2	Hyperion	0.1 × 0.1	0.0353	38.0	431.3	–	–
56-2T	Mean-ol	–	–	–	1.3	26.3	3.9	2.4
56-2T	Mean-opx	–	–	–	39.0	439.2	–	–

[a] Squared and circular aperture are noted with the form 0.1 × 0.1 and 0.105, respectively.
[b] Calibration from Paterson (1982).
[c] Calibration of Bell et al. (2003).
[d] Calibration of Withers et al. (2012).

The water concentration in the analysed minerals was calculated by integrating the absorption bands according to the calibration of Paterson (1982):

$$C_{OH} = \frac{X_i}{150\zeta}\int \frac{K(\bar{\nu})}{(3780-\bar{\nu})}d\bar{\nu}$$

where C_{OH} is the hydroxyl concentration (in H/10^6 Si or wt. ppm H_2O), ζ is an orientation factor (1/3 for unpolarized measurements), and $K(\bar{\nu})$ is the absorption coefficient in cm^{-1} for a given wavenumber $\bar{\nu}$. X_i is a density factor; its value for studied olivine, orthopyroxene and clinopyroxene is 2695, 2769, and 2705 wt. ppm H_2O, respectively (see Bolfan-Casanova et al. (2000) for calculation method). The range of integration for olivine, orthopyroxene and clinopyroxene is 3200–3400 cm^{-1}, 3000–3630 cm^{-1} and 3100–3670 cm^{-1}, respectively. Errors on the water contents are in the range of ±30% (Denis et al., 2013; Kohlstedt et al., 1996). To facilitate comparison with data in the literature, we present, in Table 3, water contents in olivine estimated with the calibration of Paterson (1982). These results may be converted, by multiplying by a factor 3, to the calibration of Bell et al. (2003) (*cf.* Férot and Bolfan-Casanova, 2012). Noteworthy, the more recent calibration by Withers et al. (2012) demonstrates that the calibration by Bell et al. (2003) overestimates the water content in olivine. However, these two most recent calibrations (Bell et al., 2003; Withers et al., 2012) may be only used for olivine spectra dominated by OH absorption bands with high wavenumbers (*i.e.*, 3650–3450 cm^{-1}) as shown by olivine hydrated at high pressure >4 GPa. This is not the case for olivine in the studied peridotites, which have spectra with dominantly low wavenumber absorption bands (Fig. 7). For that reason and because it allows direct comparison between water contents in olivine and pyroxenes (Bolfan-Casanova et al., 2000), water contents resulting from the calibration of Paterson (1982) will be used in the following analysis.

6.2. FTIR spectra and water contents

Olivine, orthopyroxene and clinopyroxene FTIR results all show evidence of OH groups incorporated in the atomic structures. Representative unpolarized FTIR spectra for olivine, orthopyroxene and clinopyroxene in xenoliths 33-2A, 54-2A, 54-2D, 55-2A, and 56-2A are shown in Fig. 8. The variations in signal to noise ratio between 3500 and 4000 cm^{-1} observed among our measurements in Fig. 8 are due to differences in the technical setup of the Bruker Hyperion and Bruker type A590 microscopes, and mostly record the quality of the clean air purge through the optics.

The major O–H absorption bands in olivine are positioned at 3355 and 3328 cm^{-1} (Fig. 8). The typical O–H absorption band group in mantle olivine between 3650 and 3450 cm^{-1} (Bell et al., 2004; Demouchy, 2004; Demouchy et al., 2006; Grant et al., 2007; Miller et al., 1987; Peslier and Luhr, 2006), often referred as group 1, is not observed. Accordingly, water contents are very low, ranging between 1 and 4 wt. ppm H_2O (Table 3).

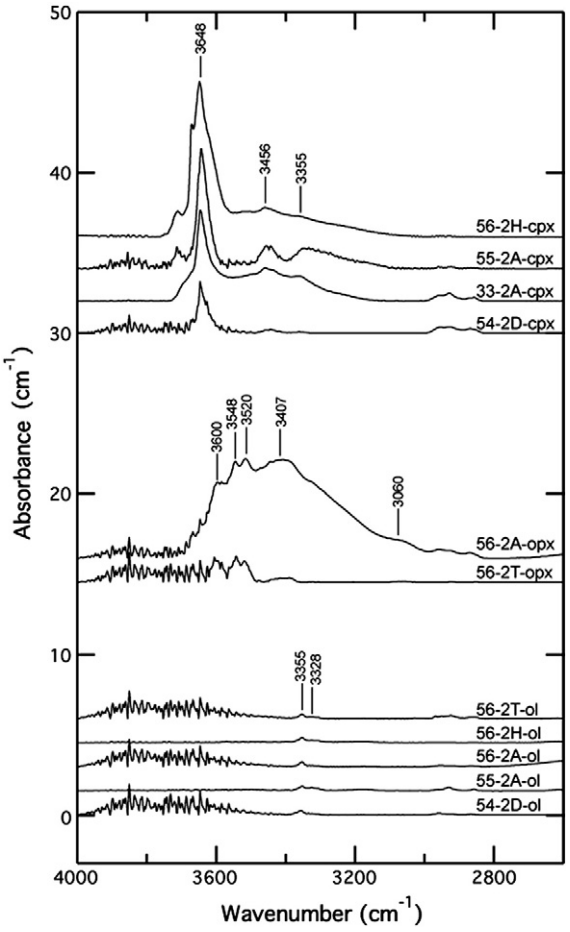

Fig. 8. Selected unpolarized FTIR spectra for olivine, orthopyroxenes and clinopyroxenes. The spectrum for orthopyroxene in the sample 56-2A is from only one measurement of a tertiary orthopyroxene. Spectra are normalized to 1 cm^{-1}.

Orthopyroxene spectra are characterized by major O–H absorption bands at 3600, 3548, 3520 and 3407 cm^{-1} and by a minor band at 3060 cm^{-1} (Fig. 8). These absorption bands are typical for orthopyroxene from mantle xenoliths (Grant et al., 2007; Peslier et al., 2002; Soustelle et al., 2010). Water contents are very heterogeneous ranging from 39 to 431 wt. ppm H_2O in samples 56-2T and 56-2A (Table 2). The sample section thickness (~300 μm) makes uneasy the comparison between the textures and the water contents in pyroxenes. Primary and secondary orthopyroxenes could not be discriminated, but it was possible to distinguish the fibrous tertiary orthopyroxenes. The lowest concentrations (38–39 wt. ppm H_2O) are observed in coarse grains from an orthopyroxene-rich layer parallel to the foliation in 56-2T; the highest concentration (431 wt. ppm H_2O) is measured in a fibrous tertiary orthopyroxene. Contents higher than 400 wt. ppm H_2O are abnormally high for orthopyroxenes from spinel peridotites, but neither optical observation nor the spectrum shows evidence of water-rich inclusions, amphibole lamellae, or contamination by water-rich glue (crystal-bond) as shown in Fig. 8. An intermediate concentration of 249 wt. ppm H_2O is measured in a coarse orthopyroxene from the lherzolite 56-2H, which contains a relatively large amount of primary pyroxenes. As the latter constitute the largest orthopyroxene crystals in that sample, this value likely represents the water concentration of primary orthopyroxenes.

Table 3
Seismic anisotropy data and elastic parameters.

	55-2B	54-2A	56-2A	55-2A	54-2D	56-2H	56-2T	33-2A
AVp (%)	16.4	13.8	12	9.5	7.9	9	8.8	5.9
Max. Avs (%)	10.51	9.64	8.02	6.29	5	6.07	5.08	3.39
AVs1 (%)	6	6.4	4.8	3.3	2.6	3.7	2.5	1.9
AVs2 (%)	7.7	6.2	5.7	5.1	4	4.1	4.4	2.5
Max Vp/Vs1	1.91	1.86	1.8	1.82	1.8	1.79	1.79	1.76
Min Vp/Vs1	1.61	1.63	1.63	1.65	1.66	1.65	1.64	1.66
Max Vp/Vs2	1.93	1.9	1.85	1.83	1.81	1.82	1.8	1.78
Min Vp/Vs2	1.74	1.73	1.71	1.73	1.73	1.71	1.72	1.7
C11	210.36	211.31	209.33	220.34	215.52	214.06	215.91	213.61
C22	291.38	277.04	266.12	262.72	265.73	255.6	256.44	227.58
C33	219.71	226.72	230.65	218.52	220.34	225.4	222.59	226.43
C44	80.27	80.65	81.7	78.95	79.07	80.18	79.61	75.54
C55	68.88	70	71.08	71.69	70.38	73.14	72.89	74.46
C66	78.55	77.46	77.94	79.36	77.77	77.33	79.08	74.36
C12	72.67	74.18	72.61	71.69	74.57	71.69	72.01	69.82
C13	77.97	76.63	75.3	74.64	77.23	73.31	73.24	70.73
C23	74.52	74.64	75.83	72.75	74.66	72.77	73.08	73.07

Clinopyroxene spectra display major O–H absorption bands at 3648, 3456 and 3355 cm^{-1} (Fig. 7). These peaks are common in natural diopside (Skogby, 2006), but the traditional peak between 3530 and 3540 cm^{-1} is not observed in our samples. The water contents in clinopyroxene are variable; it ranges from 77 to 382 wt. ppm H_2O (Table 2). Unfortunately, as explained above, because of the thickness of the double polished section and the relatively small size of the clinopyroxene crystals (below 300 μm), it was not possible to properly associate textures and water contents for this mineral. However, the lowest values (77.5 wt. ppm H_2O) have been measured in the sample 54-2D, which contains a large amount of secondary clinopyroxenes.

7. Seismic properties

The three-dimensional distribution of seismic velocities has been computed by averaging the individual grain elastic constant tensor as a function of the crystallographic orientation given by the EBSD measurements and modal composition (Mainprice and Humbert, 1994). We used Voigt–Reuss–Hill averaging and single-crystal elastic constant tensors of olivine, orthopyroxene and clinopyroxene at ambient conditions (Abramson et al., 1997; Collins and Brown, 1998; Duffy and Vaughan, 1988).

As seismic waves sample the anisotropy at length scales ranging from a few to a thousand of kilometres, we calculated seismic properties for an average peridotite sample obtained by summation of the CPO of the 7 peridotites from the studied xenolith suite. The olivine clinopyroxenite is not used since it seems unrealistic that one eighth of the mantle wedge would have a pyroxenite composition. Indeed, pyroxenites usually occur as centimetre to tens of centimetre wide layers in both xenoliths and peridotite massifs (Franz et al., 2002; Soustelle et al., 2009; Tommasi et al., 2006).

The 3D-seismic properties of the average sample (Fig. 9) are very similar to those of individual peridotite xenoliths (Online supplementary material). The main variation is in the intensity of the anisotropy. The decrease of the olivine CPO strength (J-index) with the increase of the pyroxene content observed in studied xenoliths results in a negative correlation between the maximum Vp and Vs anisotropy and the pyroxene modal content (Fig. 10). In all samples, P- and S_2-wave propagation is fastest parallel to the lineation and slowest in the plane normal to the lineation. S_1-wave velocity is minimum for propagation directions both parallel and normal to the lineation and maximum at ~45° to the lineation in the foliation plane. S-wave splitting is minimum for waves propagating at low angle to the lineation and highest for waves propagating at high angles (≥30°) to the lineation in the foliation plane. S-waves propagating normal to the foliation also sample a high birefringence direction. For all propagation directions, the fast S-wave is polarized parallel to the lineation. The Vp/Vs_1 and Vp/Vs_2 ratios are minimum for propagation directions at high angle (>30°) to the lineation and the foliation, respectively. Both ratios are maximum parallel to the lineation. This pattern is typical of peridotites with olivine CPO with an orthorhombic or axial [100] symmetry (Tommasi et al., 2004; Vauchez et al., 2005). These anisotropy patterns are also in good agreement with the seismic properties calculated for xenoliths from the Avacha volcano in Kamchatka, which represent the supra-subduction mantle (Michibayashi et al., 2009; Soustelle and Tommasi, 2010).

8. Discussion

8.1. Relative chronology of the events

Previous petrological and geochemical studies (Franz et al., 2002; Gregoire et al., 2001) have proposed that peridotite xenoliths from the Tubaf and Edison seamounts sample a lithosphere that has been affected by high degree partial melting (15–20%) at a mid-ocean ridge or a back-arc spreading centre and then drifted away and cooled (Fig. 12a). This succession of events is supported by the low cooling rates (0.1–1 °C/Ma) calculated by Franz et al. (2002) from the Ca zoning in olivine from the studied spinel peridotites. These authors assume that such low cooling rates are reached only when the oceanic lithosphere has drifted far away from the mid-ocean ridge, *i.e.* 3000 km at a half spreading rates of 6 cm/year. As McInnes et al. (1999) pointed out, based on Re–Os ages from the oceanic crust (McInnes et al., 1994), the Bismarck microplate, on which the Tubaf and Edison seamounts sit, once formed a part of the Pacific Plate, but separated from it at some time in the past. The Pacific plate was then subducted below its former fragment, forming the Manus–Kilinailau trench (Fig. 12b). Around 15 My, collision between the Ontong-Java plateau and the Bismark microplate resulted in arrest of the subduction along the Manus–Kilinailau trench and in subduction of the Solomon Sea microplate under the Bismarck microplate (Fig. 12c). Cessation of the subduction may have allowed for rapid heating and dehydration of the stalled Pacific slab (Arcay et al., 2007). Dewatering of the uppermost portion of the stalled slab was indeed

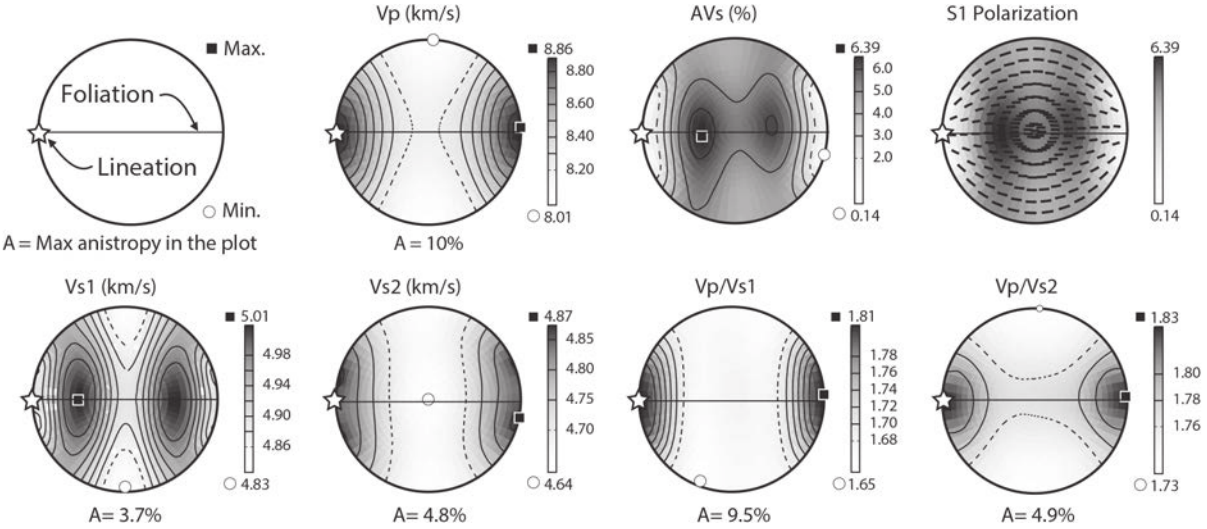

Fig. 9. Seismic properties of a mean sample obtained by the summation of the CPO and averaging of the modal composition of the 7 studied peridotite xenoliths. From left to right and top to bottom, schematic representation of the lineation and foliation reference frame used in this study, variation as a function of the propagation direction of the compressive wave velocities (Vp in $km \cdot s^{-1}$), of the shear wave polarization anisotropy (AVs in $\% = 200 \times (Vs_1 - Vs_2) / (Vs_1 + Vs_2)$), of the polarization of the fast shear wave S_1 (grey scale represent the intensity of AVs, as in the previous plot), of the two quasi-shear waves (Vs_1 and Vs_2) velocities, and of the Vp/Vs1 and Vp/Vs2 ratios. Equal area, lower hemisphere stereographic projections.

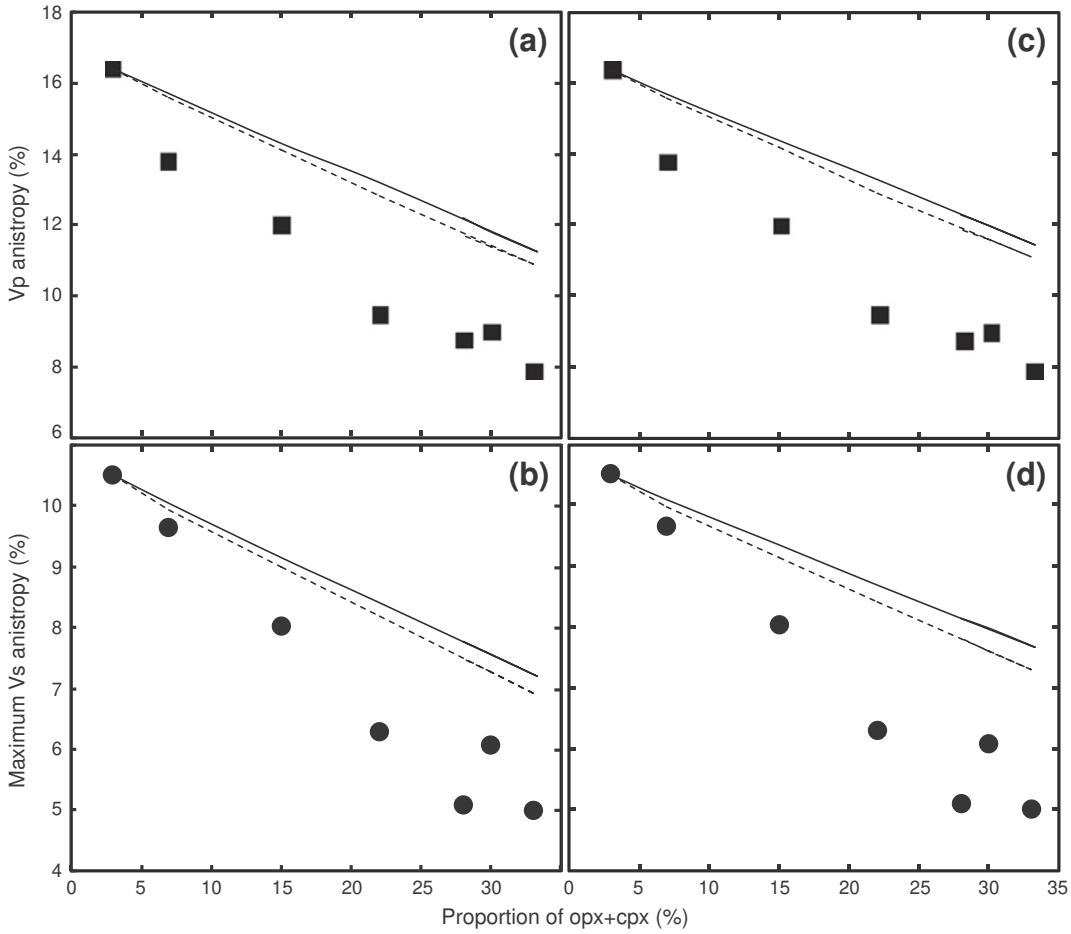

Fig. 10. Vp (a and c) and maximum Vs (b and d) anisotropy in relation to the pyroxene content. The solid and dashed lines represent the evolution of the anisotropy calculated by increasing the proportion of orthopyroxene and clinopyroxene, respectively, with either a random (a and b) or a strong (c and d) CPO. Orthopyroxene and clinopyroxene CPO used for the calculation (c and d) are from samples 55-2A and 56-2T, respectively, which have CPO relatively strong and consistent with the described deformation.

proposed to explain the extensive hydrous metasomatism recorded by the formation of phase 3 pyroxenes in veins in the studied peridotites (McInnes et al., 2001)

The studied spinel peridotites display clear evidence for ductile deformation at high temperature, such as the development of a foliation and a lineation pointed out by the alignment of spinel trails and the shape preferred orientation of coarse grained olivine crystals (Fig. 2). Olivine crystals show clear evidence for deformation by dislocation creep, such as undulose extinction, subgrain boundaries (Fig. 4), and development of a strong CPO (Fig. 6). The shape of olivine grain boundaries, which range from interlobate to smoothly curved and sometimes straight, leading to the formation of 120° triple junctions, is characteristic of dynamic recrystallization by grain boundary migration and grain boundary area reduction processes. These observations demonstrate that olivine accommodated deformation by dislocation creep at high temperature, which allows a large contribution of diffusion processes. The primary pyroxenes also display evidence for intracrystalline deformation: undulose extinction and kinks (Fig. 5a and b), as well as local 120° triple junctions indicating grain boundary migration. These textures suggest that the primary pyroxenes were submitted to the same high-temperature deformation as the olivine. The equilibrium temperatures, calculated using pyroxene rim compositions and Ca in olivine (730–980 °C; Franz et al., 2002), are nevertheless far too low to allow for the formation of the observed microstructures during deformation. Cooling from initially higher temperatures is suggested by the occurrence of exsolutions in primary pyroxenes, the decrease of Mg and the increase of Ca in primary orthopyroxene from core to rim, as well as the decrease of Ca in olivine from core to rim (Franz et al., 2002). We propose therefore that the high-temperature deformation responsible for the olivine and primary pyroxene microstructures and textures occurred either at the spreading centre or at the base of the lithosphere due to the velocity contrast between the plate and the asthenosphere and was frozen in the lithospheric mantle by the progressive cooling of the oceanic plate (Fig. 12a).

The tertiary pyroxenes mostly occur in veins that crosscut the lineation and the foliation, as well as the deformation-related microstructures in olivine, primary and secondary pyroxenes. Hence, the crystallization of these tertiary pyroxenes clearly postpones the high temperature deformation event. This is consistent with the previous interpretation by Franz et al. (2002), which related the precipitation of these pyroxenes to a late metasomatic event: the last one before sample extraction. Franz and Romer (2010) have suggested that different metasomatic agents are responsible for the crystallization of the tertiary pyroxenes, suggesting that this metasomatism implied a range of dehydration reactions during heating of the stalled Pacific Plate after the collision between the Ontong-Java plateau and the Bismarck Microplate (Fig. 12c).

Finally, the secondary pyroxenes, with their interstitial film-like shapes along olivine grain boundaries (Fig. 5d), probably result from a diffuse fluid/melt percolation in a hotter environment, probably at the base of the mantle lithosphere. This event certainly occurred between the stages 1 and 3, since the veins composed by the tertiary pyroxenes crosscut them (Fig. 5e and f) and the secondary pyroxenes display no intracrystalline deformation microstructures (Figs. 4a, 5b and d),

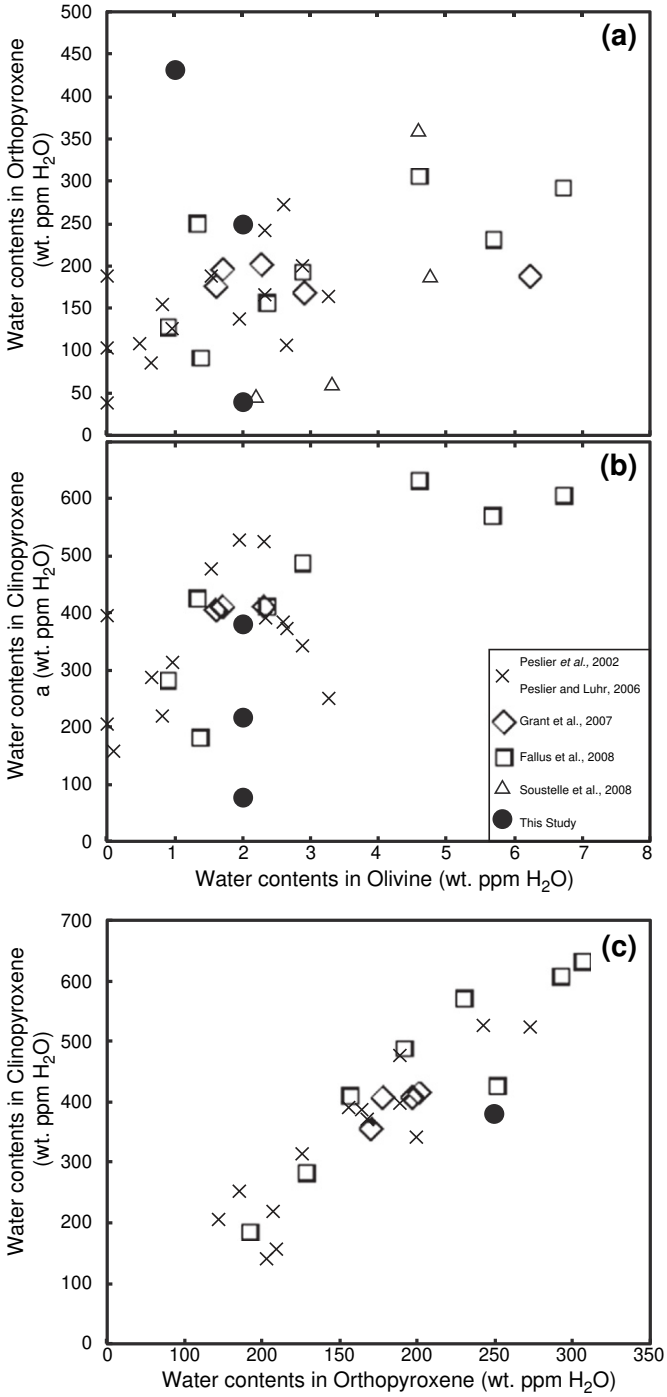

Fig. 11. Water concentration comparison between: (a) orthopyroxene and olivine; (b) clinopyroxene and olivine; (c) orthopyroxene and clinopyroxene. Olivine water concentration values are converted to the calibration of Paterson (1982).

which indicates that their crystallization postdates the high temperature deformation. We propose therefore that the secondary pyroxenes are likely the result of the metasomatism of the supra-subduction mantle above the Pacific slab, before the collision with the Ontong-Java plateau (Fig. 12b). This interpretation is similar to the one proposed by McInnes et al. (2001) to explain the pyroxenes along grain boundaries in their "type B" peridotite xenoliths extracted from the Tubaf and Edison seamounts. They have associated them to an early diffusion/percolation metasomatic event involving hydrous fluids extracted from the subducted slab.

These secondary pyroxenes occur, however, mostly in bands or lenses aligned parallel to the high-temperature foliation. This shape preferred orientation coherent with the deformation structures is usually interpreted as indicating synkinematic fluid-rock reactions, where the melt distribution is controlled by the deformation (*e.g.*, Higgie and Tommasi, 2012; Holtzman et al., 2003a; King et al., 2010; Le Roux et al., 2008; Soustelle et al., 2009, 2010). It may however also form under static, post-kinematic conditions due to an anisotropic permeability of olivine-rich rocks, characterized by an easier wetting of or preferential dissolution of olivine along (010) grain boundaries, which has been suggested based on experimental data (Boudier, 1991; Waff and Faul, 1992). This processes has been proposed, for instance, to explain the alignment of websteritic lenses parallel to the foliation in the harzburgites in the Lherz massif (Le Roux et al., 2008) and of secondary clinopyroxenes in highly annealed xenoliths with tabular textures (Tommasi et al., 2008). As olivine (010) planes are dominantly oriented in the foliation plane (Fig. 6), this anisotropic permeability might account for the formation of a compositional layering parallel to the foliation even if the reactive percolation forming the layering is post-kinematic.

The negative correlation between the proportion of pyroxene and olivine grain size and J-index (Figs. 3 and 7) favours, however, a synkinematic crystallization of the secondary pyroxenes. The smaller grain sizes in the pyroxene-rich bands may be explained by two processes: Zener pinning, which hindered olivine grain growth in these bands (Evans et al., 2001; Nes et al., 1985; Smith, 1948), or, as described in peridotite xenoliths from the Avacha volcano (Soustelle et al., 2010) and in peridotites from the Othris ophiolite (Dijsktra et al., 2002), by pyroxene crystallization at the expenses of olivine as a result of fluid or melt-rock reactions. Under static conditions, these processes should not significantly change the olivine CPO strength. The dispersion of the olivine CPO may be accounted if the fluid/melt-rock reactions producing the crystallization of the secondary pyroxenes are synkinematic as the presence of fluids along grain boundaries may allow for limited grain boundary sliding and rotation of the new isolated olivines relative to their initial "parent" orientation and then loose the orientation of the parent crystals (Soustelle et al., 2010). In conclusion, the bands or lenses composed by secondary pyroxenes aligned parallel to the high-temperature foliation and the relation between olivine J-index and the pyroxene proportion favour a model in which crystallization of the secondary pyroxenes was coeval to high-temperature deformation in the supra-subduction mantle. The metasomatism producing the secondary pyroxenes must, however, have continued under late-kinematic conditions to explain the absence of intracrystalline deformation features in the secondary pyroxenes.

8.2. Hydration of the sub-arc lithospheric mantle

The measured water contents in olivine, orthopyroxene and clinopyroxene of 1–4, 38–431 and 77–382 wt. ppm H_2O, respectively (Table 2) may be compared to the water solubility in these phases at the pressure and temperature conditions corresponding to the equilibrium conditions recorded for metasomatized and primary assemblages in our samples (650 °C–1 GPa and 980 °C–2 GPa) using the semi-empirical equation of water solubility in mantle nominally anhydrous minerals from Keppler and Bolfan-Casanova (2006):

$$C_{water} = A f_{H_2O}^{n} \exp\left(-\frac{\Delta H^{1\,bar} + \Delta V^{s} P}{RT}\right)$$

where C_{water} is the water solubility in wt. ppm H_2O, A is a constant in ppm/bar^n, f_{H_2O} is the water fugacity in bar, n is an exponent related to the dissolution mechanism of OH and considered to equal 1 for olivine, $\Delta H^{1\ bar}$ is the reaction enthalpy at 1 bar in J·mol^{-1}, ΔV^s is the volume change of the solids in m^3·mol^{-1}, P is the pressure in Pa, R is

the gas constant, and T the temperature in K. f_{H_2O} has been determined with the fugacity calculator of Withers (http://www.geo.umn.edu/people/researchers/withe012/fugacity.htm), and for A, n, $\Delta H^{1\ bar}$, and ΔV^{s} we used the values from Zhao et al. (2004), Mierdel and Keppler (2004) and Gavrilenko (2008) for olivine, orthopyroxene and clinopyroxene, respectively. The resulting water solubility in olivine, orthopyroxene and clinopyroxene at 650 °C/1 GPa and 980 °C/2 GPa are 3–82, 67–258 and 156–407 wt. ppm H_2O, respectively. The analysed olivine crystals are therefore water undersaturated. The measured water contents should however represent a minimum because of hydrogen depletion by diffusion during the extraction of the xenoliths by volcanism (Demouchy et al., 2006; Denis et al., 2013; Peslier and Luhr, 2006).

The pyroxenes show water content in the range, lower or higher (only orthopyroxene) than the theoretical saturation value. Al enrichment might explain the highest values (Mierdel et al., 2007; Rauch and Keppler, 2002), but Al_2O_3 concentration in orthopyroxene in the analysed samples is relatively low, between 0.1 and 2 wt.% of Al_2O_3 (Franz et al., 2002). The highest water content (431 wt. ppm H_2O) is measured in a tertiary orthopyroxene aggregate, composed of very small crystals in sample 56-2A (Fig. 5g). Comparable water contents have been measured in low-Al orthopyroxenes displaying similar textures in peridotite xenoliths from the Kamchatka of volcanic arc (Soustelle et al., 2010), suggesting that they are typical late, low-temperature fluid-rock reactions in subduction environments. The lowest water contents in orthopyroxene (39 wt. ppm H_2O) and clinopyroxene (77.5 wt. ppm H_2O) have been measured in samples 56-2H and 54-2D, respectively. The first has a high concentration of secondary orthopyroxenes and the second a large amount of secondary clinopyroxenes and has been described by Franz et al. (2002) as a spinel lherzolite with phlogopite-bearing clinopyroxene–olivine veins. Both samples have therefore been strongly metasomatized by Si-rich hydrous fluids or melts under relatively high oxygen fugacity condition ($D\log(fO_2)^{FMQ}$ of 2.8–4.3 for 54-2D, *cf.* Franz et al., 2002). Such conditions result in low water content in pyroxenes accordingly to Skogby and Rossman (1989) and Peslier et al. (2002). The hypothesis of a strong silica activity and high oxygen fugacity is also supported by the olivine FTIR spectra, which display major O – H absorption bands at 3355 and 3328 cm^{-1} (Berry et al., 2005; Mosenfelder et al., 2006). Finally, the pyroxenes with water contents close to the theoretical saturation values when considering the uncertainties from the empirical calibration of Paterson (Paterson, 1982) are from xenoliths 55-2A and 56-2H, which have predominantly pyroxenes with primary textures. We assume therefore that these peridotites have been less affected by the metasomatism and hence equilibrated under less oxidising conditions. This may account for the high, near-saturation water contents in pyroxenes from those two samples.

Concentration ratios between minerals (R_c) have been calculated using the mean water content for each mineral in the sample. $R_c^{cpx/ol}$ are 38.5, 111 and 180 in 54-2D, 55-2A and 56-2H, respectively. $R_c^{opx/ol}$ are 431.5, 124.5 and 19.5 in 56-2A, 56-2H and 56-2T, respectively. $R_c^{cpx/opx}$ is 1.53 in 56-2H. In sample 56-2H, the only orthopyroxene studied does not have a "clean" spectrum, thus its values of $R_c^{opx/cpx}$ and $R_c^{opx/ol}$ have to be considered carefully. The concentration ratios between minerals are highly variable from one sample to another, due to the heterogeneity of pyroxene water contents, which probably reflects disequilibrium between olivine and pyroxenes.

Despite water contents in olivine from studied xenoliths being rather low, they remain in the range of spinel peridotite xenoliths from other subduction zones as illustrated in Fig. 11a and b (*e.g.*, Demouchy et al., 2006; Denis et al., 2013; Falus et al., 2008; Grant et al., 2007; Peslier and Luhr, 2006; Peslier et al., 2002; Soustelle et al., 2010). Water contents in pyroxene in the present study are more variable and encompass the full range reported from other subduction localities (Fig. 11; Demouchy et al., 2006; Falus et al., 2008; Grant et al., 2007; Peslier and Luhr, 2006; Peslier et al., 2002; Soustelle et al., 2010). This variation may reflect the complex history responsible for the occurrence of different generations of pyroxenes. Ortho- and clinopyroxenes from the sample 56-2H are however in the trend formed by the pyroxenes from spinel peridotites of other subduction zones (Fig. 11c). We therefore assume that the water concentration in pyroxenes from 56-2H is representative of the subduction-related hydration of the upper mantle below the Lihir Island. This assumption is supported by the $R_c^{opx/cpx}$ calculated in this sample (1.53), which is consistent with the partition coefficient $D^{cpx/opx}$ experimentally determined by Aubaud et al. (2004). Calculation of water concentration in olivine using the $D^{ol/opx}$ and $D^{ol/cpx}$ from Aubaud et al. (2004), and the orthopyroxene and clinopyroxene from 56-2H water contents, yields values of 27 and 30 wt. ppm H_2O, which is in the range of the theoretical saturation values, well above the water content reported here for olivine.

8.3. CPO and seismic properties of the sub-arc lithosphere

The determination of the dominant deformation mechanisms of olivine in the upper mantle is fundamental to decipher the flow patterns in the mantle from S-waves anisotropy data. All the studied peridotites display a stronger concentration of the olivine [100] axes relatively to the [010] and [001] axes. When a mineral lineation is observed (*e.g.*, 54-2A and 56-2T, Fig. 2a and c), it is parallel to the maximum concentration of the [100] olivine axes (Fig. 6). This strongly suggests a [100] slip direction. Except for 56-2A, all samples display a girdle distribution of the [010] and [001] axes normal to the [100] maximum, but with the [010] axes always more concentrated the [001] ones. In sample 55-2A, the direction of the spinel and pyroxene-rich lenses alignment, which mark the foliation, is normal to the maximum concentration of the [010] axes. The orthopyroxene in this sample display a weak CPO, where the [100] and [001] axes show a maximum concentration at low angle with the olivine [010] and [100] axes, respectively. Under pressure and temperature appropriate to the upper mantle conditions, under low water and Al content, the dominant slip system in orthopyroxene is (100)[001] (Doukhan et al., 1986; Manthilake et al., 2013). All these observations imply that olivine deformed by dislocation on multiple [100]{0kl} slip systems, with the dominant slip plane being (010). This slip system is characteristic for deformation under high temperature, low stress, and relatively low pressure (Bai et al., 1991; Carter and Avé Lallemand, 1970; Couvy et al., 2004; Durham and Goetze, 1977; Jung and Karato, 2001; Jung et al., 2006; Mackwell et al., 1985; Raterron et al., 2007). The secondary maximum of (001) may be explained by activation of (001)[100], which is favoured by limited hydration of the olivine. The measured water content in olivine (1–4 wt. ppm H_2O) is much lower than those determined experimentally for the change in slip plane from (010) to (001) (Jung and Karato, 2001; Jung et al., 2006). However, the olivine hydration values estimated using the pyroxene water contents from sample 56-2H and olivine–orthopyroxene partition coefficients (27–30 wt. ppm H_2O) are consistent with the experimental results, and may account for significant activation of (001)[100] slip system. Harzburgite 56-2A, which has the lowest water concentration in olivine (Table 2), shows an orthorhombic olivine CPO that suggests dominant activation of a single slip system, namely the (010)[100] slip system. In conclusion, the dominant activation of both (010)[100] or (001)[100] slip system implies that the studied samples were dry to slightly hydrated during the high temperature deformation event. This together with the high variability of water contents in pyroxenes, suggests that metasomatism might have modified in a spatially heterogeneous way the water concentrations in olivine from the Bismarck microplate lithospheric mantle.

Olivine CPO displaying an [100] axial pattern imply that fast S-wave polarization and P- and Rayleigh propagation directions are parallel to the lineation and therefore to the mantle flow direction (Fig. 9). As observed for peridotite xenolith from Avacha volcano (Soustelle and Tommasi, 2010), the presence of fluids or melt during the deformation

does not have an influence on the fast S-wave polarization directions. The pyroxene enrichment, which is negatively correlated with olivine J-index (Fig. 7), results in a decrease in the maximum Vp and Vs anisotropies (Fig. 10). The anisotropy decreases by ~50% from the most depleted dunite 55-2B to the pyroxene-rich lherzolite 54-2D (Table 3). We calculated the anisotropy evolution produced by addition of preferentially or randomly orientated ortho- or clinopyroxenes; this process yields a decrease of the Vp and maximum Vs anisotropy, but does explain the present data, implying the most important effect for the anisotropy is the dispersion of the olivine CPO (Fig. 10).

Calculation of seismic properties also highlights a strong anisotropy of Vp/Vs_1 (9.5%) and Vp/Vs_2 (4.9%, Fig. 9). This ratio is very important because it may constrain the composition of the mantle wedge. The high Vp/Vs ratio may indicate the presence of fluids or melts (Takei, 2002), whereas low Vp/Vs ratios (<1.7) are classically attributed to changes in mineralogical composition. The present results, similarly to those obtained by Soustelle and Tommasi (2010) on peridotite xenoliths from the Avacha volcano, however, demonstrate that almost the whole Vp/Vs ratio range observed in the upper mantle can be explained by the intrinsic anisotropy of rocks from a mantle wedge, without any compositional change. The studied samples display indeed Vp/Vs_1 lower than 1.7 for rays propagating at more than 30° from the lineation and Vp/Vs_1 ratios as high as 1.8 for rays propagating parallel to the lineation (flow direction)

9. Conclusions

The studied mantle xenoliths extracted by the Tubaf and Edison seamounts close to the Lihir Island, in the Papua-New-Guinea archipelago may be assumed to be representative of the Bismarck microplate lithospheric mantle. They have indeed recorded a large range of the petrological, geochemical and microstructural features related to the geodynamical events that have affected the Bismarck Microplate. Detailed analysis of the textures and microstructures combined with the previous petrological and geochemical studies (Franz and Romer, 2010; Franz et al., 2002; Gregoire et al., 2001; McInnes et al., 2001) allowed us to unravel a relative chronology of deformation and metasomatic events. Olivine and primary pyroxenes recorded a high temperature deformation stage at the base of the lithosphere, which might have lasted from the initial spreading at the ridge to the subduction. During the latter, the base of the lithosphere has been likely metasomatized by the fluids resulting from the dehydration of the subducted Pacific slab. The subduction-related metasomatism may be divided in two main events: an early one related to the subduction of the Pacific Plate under the Bismarck Microplate, which was responsible for the crystallization of the secondary pyroxenes (Fig. 12b) and a more recent one associated to the cessation of the subduction of the Pacific plate due to the collision of the Ontong-Java Plateau and the start of the Solomon Sea Microplate subduction (Franz and Romer, 2010), which induced the formation of the different veins composed of tertiary pyroxenes (Fig. 12c).

The high temperature deformation induced the development of an olivine CPO consistent with high temperature, low stress and pressure, and low to moderate hydration. As a consequence, one or two slip systems were dominant, that is either (010)[100] or both (010)[100] and (001)[100] for sample with low and moderate olivine water contents, respectively. If anisotropy in the mantle wedge results essentially from olivine deformation, the fast S-wave polarization will be therefore parallel to the lineation and thus to the flow direction. Our microstructural observation also show that the fluids or melts, which have percolated the Bismarck Microplate lithosphere during this high temperature deformation event, have suffered shear-controlled segregation, reacted with the host peridotite producing crystallization of secondary pyroxene. The presence of low melt fractions during the deformation lead to a decrease of olivine CPO strength, reducing the seismic anisotropy of the peridotites by up to 50%.

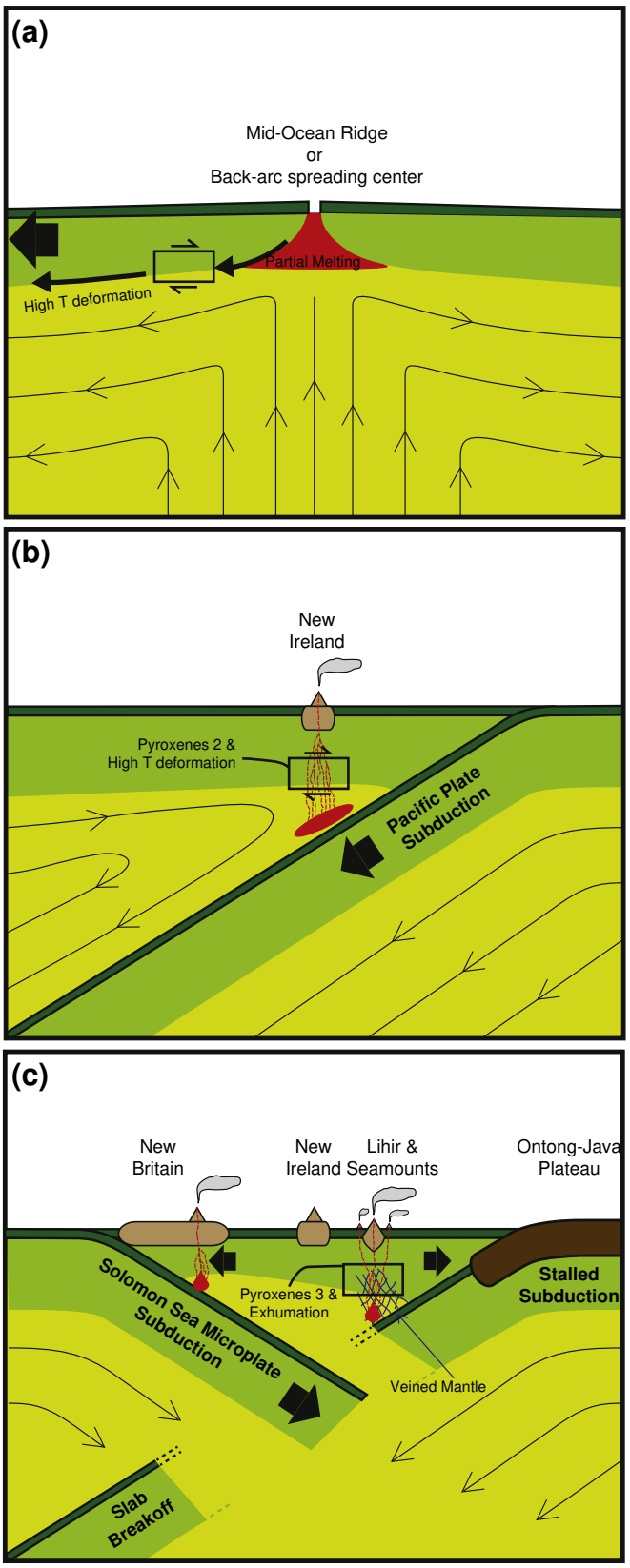

Fig. 12. Sketch of the evolution of the Bismarck Microplate lithosphere from (a) its formation at a spreading centre, to (b) the Pacific Plate subduction below the Bismarck subduction, and to (c) the cessation of the Pacific Plate subduction due to the Ontong-Java Plateau collision, the start of the Solomon Sea Microplate subduction, and the exhumation of the studied xenoliths (modified from Franz et al. (2002) and Franz and Romer (2010)). The black box gives the expected position of the studied samples and the shear directions symbolize the active deformation, not the sense of shearing.

The present observations of olivine low hydration, enrichment in pyroxenes by fluid/melt-rock reactions, and olivine CPO dispersion and their consequences to seismic anisotropy are similar to those previously made on peridotite xenoliths extracted by the Avacha volcano in the Kamchatka subduction zone (Soustelle et al., 2010). This convergence suggests that the observed fast S-wave polarization parallel to the mantle flow, the seismic anisotropy decrease and the very anisotropic and, hence, variable Vp/Vs ratios are general characteristics of the supra-subduction mantle.

Acknowledgements

We thank C. Nevado and D. Delmas, who supplied high-quality polished thin sections for EBSD and FTIR measurements. FTIR analyses were performed at Université Montpellier 2 (France) with the help of D. Maurin at the Laboratoire Colloïdes, Verres et Nanomateriaux. We thank D. Mainprice for providing software for calculating seismic properties. We acknowledge V. Le Roux and an anonymous referee for their constructive reviews. The research leading to these results has benefited from funding from the Institut National des Sciences de l'Univers — Centre National de la Recherche Scientifique (CNRS-INSU) and from the Initial Training Network (ITN) Crystal2Plate, an FP7-funded Marie Curie Action under grant agreement number PITN-GA-2008-215353.

References

Abramson, E.H., Brown, J.M., Slutsky, L.J., Zaug, J., 1997. The elastic constant s of the San Carlos olivine up to 17 GPa. J. Geophys. Res. 102, 12,252–212,263.

Arai, S., Kida, M., 2000. Origin of fine-grained peridotite xenoliths from Iraya volcano of Batan Island, Philippines: deserpentinization or metasomatism at the wedge mantle beneath an incipient arc? Island Arc 9, 458–471.

Arcay, D., Doin, M.-P., Tric, E., Bousquet, R., 2007. Influence of the precollisional stage on subduction dynamics and the buriest crust thermal state: insights from the numerical simulations. Tectonophysics 441, 27–45.

Aubaud, C., Hauri, E.H., Hirschmann, M.M., 2004. Hydrogen partition coefficient between nominally anhydrous minerals and basaltic melts. Geophys. Res. Lett. 31, L20611.

Bai, Q., Mackwell, S.J., Kohlstedt, D.L., 1991. High-temperature creep of olivine single-crystals.1. Mechanical results for buffered samples. J. Geophys. Res. Solid Earth Planets 96, 2441–2463.

Ballhaus, C., Berry, R.F., Green, D.H., 1991. High pressure experimental calibration of the olivine–orthopyroxene–spinel oxygen geobarometer: implications for the oxidation state of the upper mantle. Contrib. Mineral. Petrol. 107, 27–40.

Bell, D.R., Rossman, G.R., Maldener, J., Endisch, D., Rauch, F., 2003. Hydroxide in olivine: a quantitative determination of the absolute amount and calibration of the IR spectrum. J. Geophys. Res. Solid Earth 108, 2105–2113.

Bell, D., Rossman, G., Moore, R., 2004. Abundance and partitioning of OH in a high-pressure magmatic system: megacrysts from the Monastery kimberlite, South Africa. J. Petrol. 45, 1539–1564.

Ben Ismail, W., Mainprice, D., 1998. An olivine fabric database: an overview of upper mantle fabrics and seismic anisotropy. Tectonophysics 296, 145–158.

Bénard, A., Ionov, D.A., 2009. Veined peridotite xenoliths from the Avacha volcano, Kamchatka: fluid types and fluid-rock interaction in supra-subduction mantle. Geochim. Cosmochim. Acta 73, A108.

Berry, A.J., Hermann, J., O'Neill, H.S.C., Foran, G.J., 2005. Fingerprinting the water site in mantle olivine. Geology 33, 869–872.

Blacic, J.D., 1972. Effect of water on the experimental deformation of olivine. In: Heard, H.C., Borg, I.Y., Carter, N.L., Rayleigh, C.B. (Eds.), Flow and Fracture of Rocks. American Geophysical Union, Washington, pp. 109–115.

Bolfan-Casanova, N., Keppler, H., Rubie, D.C., 2000. Water partitioning between nominally anhydrous minerals in the MgO–SiO_2–H_2O system up to 24 GPa: implications for the distribution of water in the Earth's mantle. Earth Planet. Sci. Lett. 182, 209–221.

Boudier, F., 1991. Olivine xenocrysts in picritic magmas. Contrib. Mineral. Petrol. 109, 114–123.

Boudier, F., Baronnet, A., Mainprice, D., 2010. Serpentine mineral replacements of natural olivine and their seismic implications: oceanic lizardite versus subduction-related antigorite. J. Petrol. 51, 495–512.

Brey, G., Köhler, T., 1990. Geothermobarometry in four-phase lherzolites II. New thermobarometers, and practical assessment of existing thermobarometers. J. Petrol. 31, 1353–1378.

Bunge, H.J., 1982. Texture Analysis in Materials Sciences. Buttleworth, London.

Carter, N.L., Avé Lallemand, H.G., 1970. High temperature flow of dunite and peridotite. Geol. Soc. Am. Bull. 81, 2181–2202.

Coleman, P.J., Kroenke, L.W., 1981. Subduction without volcanism in the Solomon Island arc. Geo-Mar. Lett. 1, 129–134.

Collins, M.D., Brown, J.M., 1998. Elasticity of an upper mantle clinopyroxene. Phys. Chem. Miner. 26, 7–13.

Couvy, H., Frost, D.J., Heidelbach, F., Nyilas, K., Ungar, T., Mackwell, S., Cordier, P., 2004. Shear deformation experiments of forsterite at 11GPa–1400 degrees C in the multianvil apparatus. Eur. J. Mineral. 16, 877–889.

Demouchy, S., 2004. Water in the Earth's Interior: Thermodynamics and Kinetics of Hydrogen Incorporation in Olivine and Wadsleyite. Bayerisches Geoinstitut. Universität Bayreuth, Bayreuth 165.

Demouchy, S., Jacobsen, S.D., Gaillard, F., Stern, C.R., 2006. Rapid magma ascent recorded by water diffusion profiles in mantle olivine. Geology 34, 429–432.

Demouchy, S., Tommasi, A., Barou, F., Mainprice, D., Cordier, P., 2012. Deformation of olivine in torsion under hydrous conditions. Phys. Earth Planet. Inter. 202–203, 56–70.

Denis, C.M., Demouchy, S., Shaw, C.S., 2013. Evidence of dehydration in peridotites from Eifel Volcanic Field and estimates of the rate of magma ascent. J. Volcanol. Geotherm. Res. 258, 85–99.

Dijsktra, A.H., Drury, M.R., Vissers, R.L.M., Newman, J., 2002. On the role of melt-rock reaction in mantle shear zone formation in the Othris Peridotite Massif (Greece). J. Struct. Geol. 24, 1431–1450.

Doukhan, J.-C., Doukhan, N., Naze, L., Van Duysen, J.-C., 1986. Défauts de réseau et plasticité cristalline dans les pyroxenes: Une revue. Bull. Minér. 109, 377–394.

Duffy, T.S., Vaughan, M.T., 1988. Elasticity of enstatite and its relationships to crystal structure. J. Geophys. Res. 93, 383–391.

Durham, W.B., Goetze, C., 1977. Plastic-flow of oriented single-crystals of olivine. 1. Mechanical data. J. Geophys. Res. 82, 5737–5753.

Evans, B., Renner, J., Hirth, G., 2001. A few remarks on kinetics of static grain growth in rocks. Int. J. Earth Sci. 90, 88–103.

Faccenda, M., Burlini, L., Gerya, T.V., Mainprice, D., 2008. Fault-induced seismic anisotropy by hydration in subduction oceanic plates. Nature 455, 1097–1110.

Falus, G., Tommasi, A., Ingrin, J., Szabo, C., 2008. Deformation and seismic anisotropy of the lithospheric mantle in the southeastern Carpathians inferred from the study of mantle xenoliths. Earth Planet. Sci. Lett. 272, 50–64.

Férot, A., Bolfan-Casanova, N., 2012. Water storage capacity in olivine and pyroxene to 14 GPa: implications for the water content of the Earth's upper mantle and nature of seismic discontinuities. Earth Planet. Sci. Lett. 349, 218–230.

Franz, L., Romer, R.L., 2010. Different styles of metasomatic veining in ultramafic xenoliths from the Tubaf seamount (Bismarck Microplate, Papua New Guinea). Lithos 114, 30–53.

Franz, L., Wirth, R., 2000. Spinel inclusion in olivine of peridotite xenoliths from Tubaf seamount (Bismark Archipelago/Papua New Guinea): evidence for the thermal and tectonic evolution of the oceanic lithosphere. Contrib. Mineral. Petrol. 140, 283–295.

Franz, L., Becker, K.-P., Kramer, W., Herzig, M., 2002. Metasomatic mantle xenoliths from the Bismarck microplate (Papua New Guinea) — thermal evolution, geochemistry and extent of slab-induced metasomatism. J. Petrol. 43, 315–343.

Gavrilenko, P., 2008. Water Solubility in Diopside. Universität Bayreuth, Bayreuth 133.

Grant, K., Ingrin, J., Lorand, J., Dumas, P., 2007. Water partitioning between mantle minerals from peridotite xenoliths. Contrib. Mineral. Petrol. 154, 15–34.

Gregoire, M., McInnes, B.I.A., O'Reilly, S.Y., 2001. Hydrous metasomatism of oceanic sub-arc mantle, Lihir, Papua New Guinea — part 2. Trace element characteristics of slab-derived fluids. Lithos 59, 91–108.

Hammond, W., Humphreys, E.D., 2000. Upper mantle seismic wave velocity: effects of realistic partial melt geometries. J. Geophys. Res. 105, 10,975–910,986.

Herzig, P., Hannington, M., McInnes, B., Stoffers, P., Villinger, H., Seifert, R., Binns, R., Liebe, T., 1994. Submarine volcanism and hydrothermal venting studied in Papua, New Guinea. Eos, Trans. Amer. Geophys. Union 75, 513–516.

Herzig, P.M., Hannington, M.D., Stoffers, P., Becker, K.-P., Drischel, M., Franklin, J., Franz, L., Gemmel, J.B., Hoeppner, B., Horn, C., Horz, K., Jellineck, T., Jonasson, I.R., Kia, P., Nickelsen, S., Percival, J., Perfit, M., Petersen, S., Schmidt, M., Seifert, R., Thießen, O., Turkay, M., Tunnicliffe, V., Winn, K., 1998. Petrology, gold mineralization and biological communities at shallow submarine volcanoes of the New Ireland fore-arc (Papua New Guinea): preliminary results of R/V Sonne cruise SO-133. Inter Ridge News, 7 34–38.

Higgie, K., Tommasi, A., 2012. Feedbacks between deformation and melt distribution in the crust–mantle transition zone of the Oman ophiolite. Earth Planet. Sci. Lett. 359–360, 61–72.

Hirth, G., Kohlstedt, D.L., 1995a. Experimental constraints on the dynamics of the partially molten upper-mantle-deformation in the diffusion creep regime. J. Geophys. Res. Solid Earth 100, 1981–2001.

Hirth, G., Kohlstedt, D.L., 1995b. Experimental constraints on the dynamics of the partially molten upper-mantle.2. Deformation in the dislocation creep regime. J. Geophys. Res. Solid Earth 100, 15441–15449.

Holtzman, B.K., Kohlstedt, D.L., Zimmerman, M.E., Heidelbach, F., Hiraga, T., Hustoft, J., 2003a. Melt segregation and strain partitioning: implications for seismic anisotropy and mantle flow. Science 301, 1227–1230.

Holtzman, B.K., Groebner, N.J., Zimmerman, M.E., Ginsberg, S.B., Kohlstedt, D.L., 2003b. Stress-driven melt segregation in partially molten rocks. Geochem. Geophys. Geosyst. http://dx.doi.org/10.1029/2001GC000258.

Ionov, D.A., 2010. Petrology of mantle wedge lithosphere: new data on supra-subduction zone peridotite xenoliths from the Andesitic Avacha Volcano, Kamchatka. J. Petrol. 51, 327–361.

Ionov, D.A., Seitz, H.-M., 2008. Lithium abundances and isotopic compositions in mantle xenoliths from subduction and intra-plate settings: mantle sources vs. eruption histories. Earth Planet. Sci. Lett. 266, 316–331.

Ishimaru, S., Arai, S., Ishida, Y., Shirasaka, M., Okrugin, V., 2007. Melting and multi-stage metasomatism in the mantle wedge beneath a frontal arc inferred from highly depleted peridotite xenoliths from the Avacha volcano, Southern Kamchatka. J. Petrol. 48, 395–433.

Jung, H., Karato, S., 2001. Water-induced fabric transitions in olivine. Science 293, 1460–1463.
Jung, H., Katayama, I., Jiang, Z., Hiraga, I., Karato, S., 2006. Effect of water and stress on the lattice-preferred orientation of olivine. Tectonophysics 421, 1–22.
Karato, S., 2002. Mapping water content in the upper mantle. In: Eiler, J., Abers, G. (Eds.), The Subduction Factory.
Karato, S., Jung, H., 1998. Water, partial melting and the origin of the seismic low velocity and high attenuation zone in the upper mantle. Earth Planet. Sci. Lett. 157, 193–207.
Karato, S.I., Paterson, M.S., Fitz Gerald, J.D., 1986. Rheology of synthetic olivine aggregates — influence of grain-size and water. J. Geophys. Res. Solid Earth Planets 91, 8151–8176.
Keppler, H., Bolfan-Casanova, N., 2006. Thermodynamics of water solubility and partitioning. In: Keppler, H., Smyth, J.R. (Eds.), Water in Nominally Anhydrous Minerals. Geochemical society & Mineralogical society of America, Chantilly (Vir.), pp. 193–230.
King, D.S.H., Zimmerman, M.E., Kohlstedt, D.L., 2010. Stress-driven melt segregation in partially molten olivine-rich rocks deformed in torsion. J. Petrol. 51, 21–42.
Kneller, E.A., van Keken, P.E., 2008. The effects of three-dimensional slab geometry on deformation in the mantle wedge: implications for shear wave anisotropy. Geochem. Geophys. Geosyst. 9, Q01003. http://dx.doi.org/10.1029/2007GC001677.
Köhler, T., Brey, G.P., 1990. Calcium exchange between olivine and clinopyroxenes calibrated as a geothermometer for natural peridotites from 2 to 60 kb with applications. Geochim. Cosmochim. Acta 54, 2375–2388.
Kohlstedt, D.L., Keppler, H., Rubie, D.C., 1996. Solubility of water in the alpha, beta and gamma phases of $(Mg, Fe)(2)SiO_4$. Contrib. Mineral. Petrol. 123, 345–357.
Le Roux, V., Tommasi, A., Vauchez, A., 2008. Feedback between melt percolation and deformation in an exhumed lithosphere–asthenosphere boundary. Earth Planet. Sci. Lett. 274, 401–413.
Licence, P.S., Terril, J.E., Fergusson, L.J., 1987. Epithermal gold mineralisation, Amnittle Island, Papua New Guinea. Proceedings of the Pacific Rim Conference '87. Australian Institute of Mining and Metallurgy, Melbourne, pp. 273–278.
Mackwell, S.J., Kohlstedt, D.L., Paterson, M.S., 1985. The role of water in the deformation of olivine single-crystals. J. Geophys. Res. Solid Earth Planets 90, 1319–1333.
Mainprice, D., Humbert, M., 1994. Methods of calculating petrophysical properties from lattice preferred orientation data. Surv. Geophys. 15, 575–592.
Manthilake, M.A.G.M., Miyajima, N., Heidelbach, F., Soustelle, V., Frost, D.J., 2013. The effect of aluminum and water on the development of deformation fabrics of orthopyroxene. Contrib. Mineral. Petrol. 165, 495–505.
McInnes, B.I.A., 1992. A Glimpse of Ephemeral Subduction Zone Processes From Simberi island, Papua New Guinea. University of Ottawa 235.
McInnes, B.I.A., Cameron, E.M., 1994. Carbonated, alkaline metasomatic melts from a subarc environment: mantle wedge from the Tabar–Lihir–Feni arc, Papua New Guinea. Earth Planet. Sci. Lett. 122, 125–141.
McInnes, B., Herzig, P., Hannington, M., Binns, R., 1994. Modern oceanic fore-arc lithosphere resembles ophiolite sequences. Eos, Trans. Amer. Geophys. Union 75, 747.
McInnes, B.I.A., McBride, J.S., Evans, N.J., Lambert, D.D., Andrew, A.S., 1999. Osmium isotope constraints on ore metal recycling in subduction zones. Science 286, 512–517.
McInnes, B.I.A., Gregoire, M., Binns, R.A., Herzig, P.M., Hannington, M.D., 2001. Hydrous metasomatism of oceanic sub-arc mantle, Lihir, Papua New Guinea: petrology and geochemistry of fluid-metasomatised mantle wedge xenoliths. Earth Planet. Sci. Lett. 188, 169–183.
Mei, S., Kohlstedt, D.L., 2000a. Influence of water on plastic deformation of olivine aggregates 1. Diffusion creep regime. J. Geophys. Res. Solid Earth 105, 21457–21469.
Mei, S., Kohlstedt, D.L., 2000b. Influence of water on plastic deformation of olivine aggregates 2. Dislocation creep regime. J. Geophys. Res. Solid Earth 105, 21471–21481.
Mei, S., Bai, W., Hiraga, T., Kohlstedt, D.L., 2002. Influence of melt on the creep behavior of olivine–basalt aggregates under hydrous conditions. Earth Planet. Sci. Lett. 201, 491–507.
Michibayashi, K., Oohara, T., Satsukawa, T., Ishimaru, S., Arai, S., Okrugin, V., 2009. Rock seismic anisotropy of the low-velocity zone beneath the volcanic front in the mantle wedge. Geophys. Res. Lett. 36, L12305. http://dx.doi.org/10.1029/2009GL038527.
Mierdel, K., Keppler, H., 2004. Temperature dependence of water solubility in enstatite. Contrib. Mineral. Petrol. 148, 305–311.
Mierdel, K., Keppler, H., Smyth, J.R., Langenhorst, F., 2007. Water solubility in aluminous orthopyroxene and the origin of Earth's asthenosphere. Science 315, 364–368.
Miller, G.H., Rossman, G.R., Harlow, G.E., 1987. The natural occurrence of hydroxide in olivine. Phys. Chem. Miner. 14, 461–472.
Moore, A.C., 1970. Descriptive terminology for the textures for rocks in granulite facies terranes. Lithos 3, 123–127.
Mosenfelder, J.L., Sharp, T.G., Asimow, P.D., Rossman, G.R., 2006. Hydrogen incorporation in natural mantle olivines. In: Jacobsen, S., Lee, S. (Eds.), Earth's Deep Water Cycle. American Geophysical Union, pp. 45–56.
Nakajima, J., Hasegawa, A., 2004. Shear-wave polarization anisotropy and subduction-induced flow in the mantle wedge of northeastern Japan. Earth Planet. Sci. Lett. 225, 365–377.
Nes, E., Ryum, N., Hunderi, O., 1985. On Zener drag. Acta Metall. 33.
Passchier, C., Trouw, R.J., 2005. Microtectonics. Springer Verlag, Berlin, Heidelberg.
Paterson, M.S., 1982. The determination of hydroxyl by infrared absorption in quartz, silicate-glasses and similar materials. Bull. Minér. 105, 20–29.
Peslier, A., Luhr, J., 2006. Hydrogen loss from olivines in mantle xenoliths from Simcoe (USA) and Mexico: mafic alkalic magma ascent rates and water budget of the subcontinental lithosphere. Earth Planet. Sci. Lett. 242, 302–319.
Peslier, A.H., Luhr, J.F., Post, J., 2002. Low water contents in pyroxenes from spinel-peridotites of the oxidized, sub-arc mantle wedge. Earth Planet. Sci. Lett. 201, 69–86.
Pollack, H.N., Chapman, D.S., 1977. On the regional variation of heat flow, geotherms, and lithospheric thickness. Tectonophysics 38, 279–296.
Raterron, P., Chen, J., Li', L., Weidner, D., Cordier, P., 2007. Pressure-induced slip-system transition in forsterite: single-crystal rheological properties at mantle pressure and temperature. Am. Mineral. 92, 1436–1445.
Rauch, M., Keppler, H., 2002. Water solubility in orthopyroxene. Contrib. Mineral. Petrol. 143, 525–536.
Rytuba, J.J., McKee, E.H., Cox, D., 1993. Geochronology and geochemistry of the Ladolam gold deposit, Lihir island, and gold deposits and volcanoes of Tabar and Tatau, Papua New Guinea. U.S. Geol. Surv. Bull. 2039, 119–126.
Sato, H., Sacks, T., Murase, G., 1989. The use of laboratory velocity data for estimating temperature and partial melt fraction in the low velocity zone: comparison with heat flow data and electrical conductivity studies. J. Geophys. Res. 94, 5689–5704.
Schmeling, H., 1985. Numerical models on the influence of partial melt on elastic, anelastic and electric properties of rocks. PartI: elasticity and anelasticity. Phys. Earth Planet. Inter. 41, 34–57.
Skogby, H., 2006. Water in natural mantle minerals I: pyroxenes. In: Keppler, H., Smyth, J.R. (Eds.), Water in Nominally Anhydrous Minerals. Geochemical society & Mineralogical society of America, Bayreuth Boulder, pp. 155–167.
Skogby, H., Rossman, G.R., 1989. OH — in pyroxene: an experimental study of incorporation mechanisms and stability. Am. Mineral. 74, 1059–1069.
Smith, C.S., 1948. Grains, phases, and interfaces: an interpretation of microstructures. Trans. AIME 175, 15–51.
Soustelle, V., Tommasi, A., 2010. Seismic properties of the supra-subduction mantle: constraints from peridotite xenoliths from the Avacha volcano, southern Kamchatka. Geophys. Res. Lett. 37, L13307.
Soustelle, V., Tommasi, A., Bodinier, J.-L., Garrido, C.J., Vauchez, A., 2009. Deformation and reactive melt transport in the mantle lithosphere above a large-scale partial melting domain: the Ronda peridotite massif, S Spain. J. Petrol. 50, 1235–1266.
Soustelle, V., Tommasi, A., Demouchy, S., Ionov, D.A., 2010. Deformation and fluid–rock interaction in the supra-subduction mantle: microstructures and water contents in peridotite xenoliths from the Avacha Volcano, Kamchatka. J. Petrol. 51, 363–394.
Takei, Y., 2002. Effect of pore geometry on Vp/Vs: from equilibrium geometry to crack. J. Geophys. Res. 107, 2043.
Taylor, B., 1979. Bismarck sea: evolution of a back-arc basin. Geology 7, 171–174.
Tommasi, A., Mainprice, D., Canova, G., Chastel, Y., 2000. Viscoplastic self-consistent and equilibrium-based modeling of olivine lattice preferred orientations: implications for the upper mantle seismic anisotropy. J. Geophys. Res. Solid Earth 105, 7893–7908.
Tommasi, A., Godard, M., Coromina, G., Dautria, J.M., Barsczus, H., 2004. Seismic anisotropy and compositionally induced velocity anomalies in the lithosphere above mantle plumes: a petrological and microstructural study of mantle xenoliths from French Polynesia. Earth Planet. Sci. Lett. 227, 539–556.
Tommasi, A., Vauchez, A., Godard, M., Belley, F., 2006. Deformation and melt transport in a highly depleted peridotite massif from the Canadian Cordillera: implications to seismic anisotropy above subduction zones. Earth Planet. Sci. Lett. 252, 245–259.
Tommasi, A., Vauchez, A., Ionov, D.A., 2008. Deformation, static recrystallization, and reactive melt transport in shallow subcontinental mantle xenoliths (Tok Cenozoic volcanic field, SE Siberia). Earth Planet. Sci. Lett. 272, 65–77. http://dx.doi.org/10.1016/j.epsl.2008.04.020.
Vauchez, A., Dineur, F., Rudnick, R., 2005. Microstructure, texture and seismic anisotropy of the lithospheric mantle above a mantle plume: insights from the Labait volcano xenoliths (Tanzania). Earth Planet. Sci. Lett. 232, 295–314.
Waff, H.S., Faul, U.H., 1992. Effects of crystalline anisotropy on fluid distribution in ultramafic partial melts. J. Geophys. Res. 97, 9003–9014.
Wagner, L.S., Beck, S., Zandt, G., Ducea, M.N., 2006. Depleted lithosphere, cold, trapped asthenosphere, and frozen melt puddles above the flat slab in central Chile and Argentina. Earth Planet. Sci. Lett. 245, 289–301.
Withers, A.C., Bureau, H., Raepsaet, C., Hirschmann, M.M., 2012. Calibration of infrared spectroscopy by elastic recoil detection analysis of H in synthetic olivine. Chem. Geol. 334, 92–98.
Zhang, H., Thurber, C.H., Shelly, D., Ide, S., Beroza, G.C., Hasegawa, A., 2004. High-resolution subducting-slab structure beneath northern Honshu, Japan, revealed by double-difference tomography. Geology 32, 361–364.
Zhao, Y.H., Ginsberg, S.B., Kohlstedt, D.L., 2004. Solubility of hydrogen in olivine: dependence on temperature and iron content. Contrib. Mineral. Petrol. 147, 155–161.
Zimmerman, M.E., Kohlstedt, D.L., 2004. Rheological properties of partially molten lherzolite. J. Petrol. 45, 275–298.